Evolution of an ancient VMS ore-forming system recorded by pyrite and sphalerite mineral texture, trace elements, and sulfur isotope: A case study from the Huangtupo Cu-Zn (-Au) deposit, Eastern Tianshan, NW China

Bingke Sun [a], Xinbiao Lv [a,b], Shouguo Wang [b], Thomas Ulrich [c], Zhihui Dai [d], Banxiao Ruan [b,*]

[a] Faculty of Earth Resources, China University of Geosciences, Wuhan 430074, China
[b] Institute of Geological Survey, China University of Geosciences, Wuhan 430074, China
[c] Department of Geosciences, Aarhus University, Høegh-Guldbergs Gade 2, DK-8000 Aarhus C, Denmark
[d] State Key Laboratory of Deposit Geochemistry, Institute of Geochemistry, Chinese Academy of Sciences, Guiyang 550081, China

ABSTRACT

The Huangtupo Cu-Zn (-Au) volcanogenic massive sulfide deposit is hosted in a suite of Early Paleozoic basic to acidic volcanic, volcaniclastic rocks in the Eastern Tianshan orogen, northwest China. The Cu-Zn orebodies are characterized by the zoning of metallogenic elements upward from a deep stockwork mineralized zone (Cu > Zn) to a shallow massive mineralized zone (Zn > Cu). Detailed petrographic and LA-ICP-MS analyses have identified five types of pyrite and three types of sphalerite. These sulfides can be distinguished in a paragenesis with four stages of sulfide mineralization. The preore stage (SI) from the deep volcanic rock contains subhedral-euhedral pyrite (Py1) with high trace element contents (e.g., Co, Ni, and Ti; Average value of total trace elements: 16764 ppm), except for Sb, and Tl, indicating a euxinic and high-temperature environment. Both the disseminated and veined pyrite (Py2) from the early ore stage (SII; stockwork zone) and the euhedral pyrite (Py3) from the main ore stage-1 (SIII-1) have a similar chemical signature, suggesting that they precipitated under similar physico-chemical conditions. These two paragenetic stages of pyrite contributed only minimally to the trace elements endowment, except for higher Se contents. The continuous convection of hydrothermal fluids caused a large accumulation of copper and zinc, forming massive orebodies. Pyrite within the Zn(Cu)-rich zone of the main ore stage-2 (SIII-2) comprises three sub-generations (Py4a ∼ c) which are characterized by enrichment in most trace elements such as Au, As, Cu, and Sb. Pyrite 4a ∼ c formed in a fluctuating sedimentary environment and recorded the injection of a short-term, gold-rich fluid, which dissolved and reprecipitated trace elements from earlier ores and surrounding rocks. Orebody deformation and local metamorphism played a key role in this gold enrichment event. Pyrite (Py5) from the late ore stage (SIV) is deficient in most elements but relatively enriched in Co, Ni, and Se. Three stages of sphalerite associated with the Py3 ∼ 4 have been distinguished in the SIII. From Sp1 to Sp3, the content of Fe, Ge, Mo, and Cd decreased gradually, but the Sp2 is relatively depleted in Ag, As, Au, Pb, and Sb compared to Sp1 and Sp3. The sensitive variation of As, Co, Ni, Se, Pb in pyrite and Fe, Cu, Mn, Sb, Cd in sphalerite provide significant information for reconstructing the hydrothermal evolution process. The sulfur isotopes of these pyrites determined by in situ LA-multicollector (MC)-ICP-MS analyses are concentrated around 0‰, but vary significantly from −2.3 to 5.8‰. The $\delta^{34}S$ values of the sphalerite range from −3.5 to 4.0 ‰ and tends to decrease from Sp1 to Sp3. These results show that the metals of the SIII were most likely derived from the deep-seated Early Paleozoic subvolcanic intrusion and Daliugou Formation during the evolution of regional island arcs.

Combining the chemical, and isotopic data and geological features, the ore-forming process of an ancient VMS deposit was deduced. These results constrain the texture, composition and sulfur isotopic signatures of sulfides in veins and deformed ore bodies, as well as the gold enrichment mechanism, and also reflect the vertical variation of trace elements at the scale of VMS deposits, supporting the existence of multiple depositional mechanisms.

* Corresponding author at: China University of Geosciences, 388 Lumo Road, Hongshan District, Wuhan, China.
  E-mail address: bxruan@foxmail.com (B. Ruan).

1. Introduction

Volcanogenic massive sulfide (VMS) deposits are one of the most important sources of metals (mainly Cu, Zn, Pb ± Au) in the world (Mercier-Langevin et al., 2011; Hannington, 2014; de Ronde et al., 2019). Metallogenesis of this kind of deposit is often complex and multistage, making it difficult for ore geologists to obtain detailed ore-forming information. Recent studies have shown that some sulfide mineral assemblages and trace elements can be excellent indicators for reconstructing hydrothermal evolutionary conditions (e.g., Duuring et al., 2016; Lee et al., 2019). For example, some mineral assemblages and micro-textures can indirectly reveal changes in the temperature, pH, and oxidation state of the ore-forming fluid (e.g., Barker et al., 2009; Deditius et al., 2011; Keith et al., 2016a; b; Gregory et al., 2019; Martin et al., 2021). Geochemical signatures of these sulfide minerals, especially pyrite and sphalerite, provide a good proxy to describe metallogeny, which includes trace element distribution among co-genetic sulfides, mineral replacement processes and processes constituted by hydrothermal fluid-flow events (e.g., Genna and Gaboury, 2015; Lee et al., 2019; Gregory et al., 2019; Li et al., 2021).

Pyrite and sphalerite are the most common metallic sulfide mineral assemblage observed in many VMS deposits. They have the ideal chemistry properties of FeS_2 and ZnS, respectively; however, pure pyrite and sphalerite are rarely found in natural samples (Abraitis et al., 2004; Belissont et al., 2014; Frenzel et al., 2016). Minor and trace elements are commonly substituted into their simple crystal structure, or wrapped as nanoparticles or micro-inclusions (Benedetto et al., 2005; Deditius et al., 2011). For example, numerous studies have revealed that pyrite can contain significant concentrations of Cu, Pb, Zn, Au, Ag, Cd, Mn, Co, Ni,

As, Sb, Se, and other elements. Metals and metalloids have been observed in pyrite as structurally bound elements or as micro- to nanoscale mineral inclusions (Deditius et al., 2014; Genna and Gaboury, 2015; Keith et al., 2016a, b; Román et al., 2019). Elements such as Pb, Ag and Cu may be present both in the sphalerite lattice and as micro-inclusions (Huston et al., 1995; Cook et al., 2009; Belissont et al., 2014; Frenzel et al., 2016). The microstructural and compositional features of pyrite and sphalerite can not only reflect the selective distribution of elements during their growth, but also be valuable in reconstructing the spatial and temporal evolution of ore-forming fluids (e.g., Reich et al., 2013; Gregory et al., 2014, 2016; Román et al., 2019; Zhuang et al., 2019). For example, changes in the texture or composition of some sulfides, especially pyrite, can also provide significant information on gold enrichment processes which has been verified in many types of gold deposits (i.e., Carlin-type and orogenic-type gold deposits; Large et al., 2009; Wu et al., 2018). Current applications of pyrite and sphalerite in VMS deposits are mainly on the scale of sulfide chimneys in well-preserved or modern VMS environments (Kristall et al., 2011), and less emphasis is placed on the use of detailed ore mineralogy (e.g., pyrite and sphalerite) in conjunction with in situ mineralogical and isotopic data to constrain the evolution of the entire VMS hydrothermal system (Genna and Gaboury, 2015; Keith et al., 2016a; Martin et al., 2021; Brueckner et al., 2021), which provide vital insights into the processes involved for deposit formation and the applied deposit model.

The Huangtupo Cu-Zn (Au) deposit (including the Honghai deposit) is the first Early Paleozoic VMS deposit in the Eastern Tianshan orogenic belt (ETOB) discovered in recent years (Fig. 1). Previous studies have conducted generalized chronological, petrogeochemical, and isotopic studies of the deposit (e.g., Mao et al., 2014; Huang et al., 2018; Yang
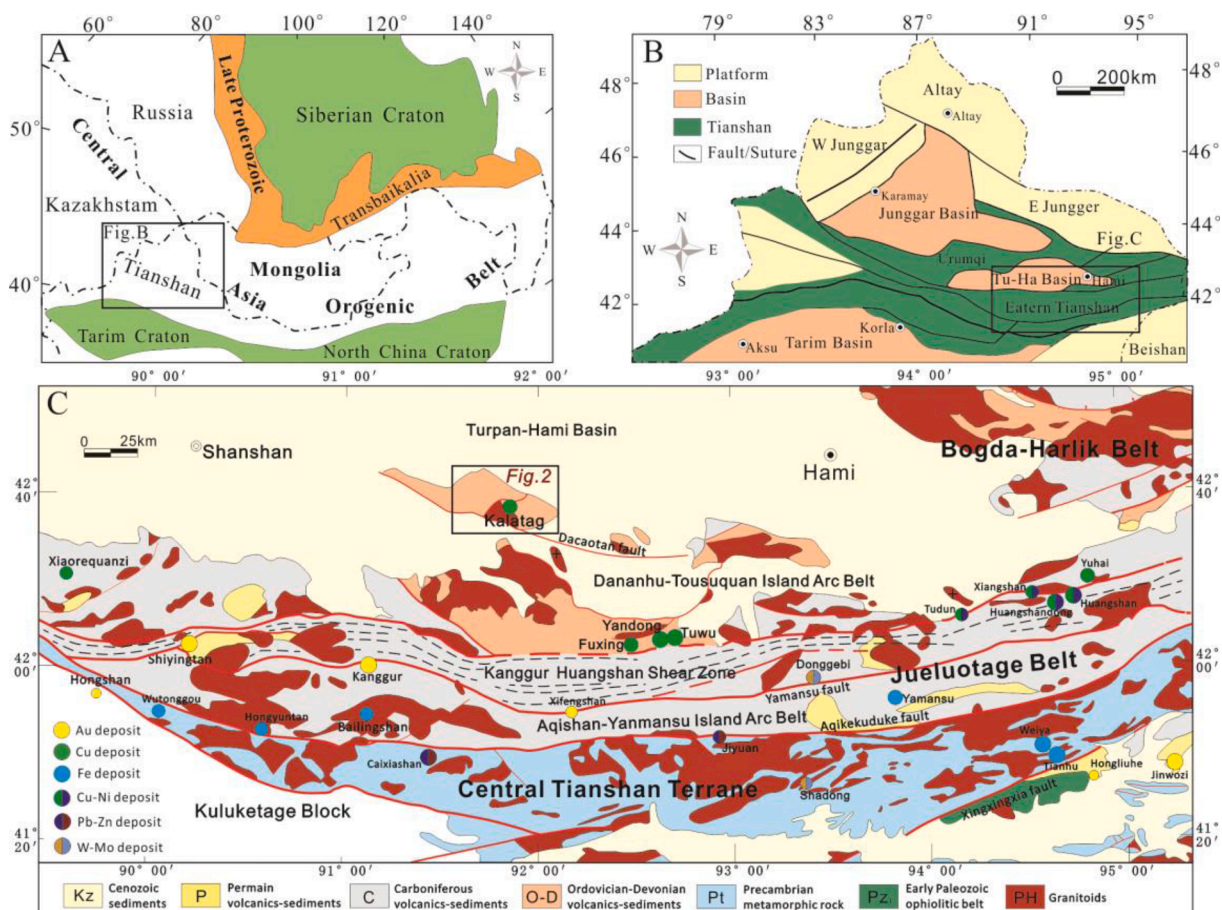

Fig. 1. A. Location of the study area in the Central Asia Orogenic Belt (modified from Sengör et al., 1993); B. Sketch map showing the geological units of the Tianshan Belt (modified from Mao et al., 2015); C. Simplified geological map of the Eastern Tianshan Belt (modified from Deng et al., 2016).

et al., 2018; Cheng et al., 2020), whereas detailed studies of mineralogical and metallogenic process evolution of the VMS system, and possible elemental (re)-mobilization (especially Au) are lacking. The application and development of mineralogy in the study of mineral deposits allow the mineral geochemistry of pyrite and sphalerite to serve as a proxy to a further detailed understanding of the nature and evolution of mineralized systems (Pfaff et al., 2011; Belissont et al., 2014). Quantitative LA-ICP-MS element distribution analysis represents a relatively new and powerful approach to assessing ore-forming processes such as in Au-Cu-Zn mineralization. Pyrite and sphalerite are the most dominant sulfides in each metallogenic stage of the Huangtupo deposit, occupying more than 90% of the sulfide in the orebody. They can be used to unravel important physical and chemical information before and after mineralization.

In this contribution, we present a detailed petrographic study of the Huangtupo deposit with particular attention to the textural and geochemical evolution of sulfide minerals. Geochemical data for different generations of pyrite and sphalerite were assessed by LA-ICP-MS and EPMA in spot and imaging analysis to reveal the distribution and evolution of metallogenic associated trace elements. In addition, in situ sulfur isotope (δ^{34}S) analysis was performed on different generations of sulfides to observe the compositional changes during mineralization and to determine the origin of sulfur and metals. These data were used to track the vertical evolution of the ore fluids composition and the processes leading to metal deposition, as well as to constrain the effects of superimposed deformation on the transport and enrichment of elements such as gold.

2. Regional geology

The Chinese ETOB has been considered as a part of the southern margin of the Central Asian Orogenic Belt (CAOB) and is located between the Junggar Basin in the north and the Tarim Basin in the south, and was formed by multiple subduction-accretion of island arcs, oceanic plateau, seamounts, ophiolites, and microcontinents during the Paleozoic (Fig. 1A, B; Goldfarb et al., 2014; Zhang et al., 2018). From south to north, it can be divided into three major tectonic zones with different rock assemblages and distinctive mineralization: the Central Tianshan Terrane, the Jueluotage belt, and the Bogda–Harlik belt (Fig. 1C; Pirajno et al., 2011).

The Jueluotage Belt is distinguished by volcanic and sedimentary layers of the Ordovician to Carboniferous age. The E-trending regional-scale Aqikuduke, Kanggur, Yamansu, and Dacaotan faults divide this belt into three tectonic subunits, including the Aqishan-Yamansu island arc belt, the Kanggur - Huangshan ductile shear zone, and the Dananhu-Tousuquan island arc belt from south to north (Fig. 1C).

The Dananhu-Tousuquan belt is situated in the northern part of the Jueluotage belt. It is an E-W trending Paleozoic island arc belt, developing a set of Ordovician to Devonian marine strata, consisting of basic-intermediate-acid volcanic rocks, pyroclastic rocks, clastic rocks, limestone, and turbidite. These rocks were generally subjected to weak metamorphism of low greenschist facies. Carboniferous-Permian mafic to intermediate lava with some clastic sandstones and conglomerates, unconformably overlay these strata (Zhang et al., 2018). This belt contains multiple types of deposits, including porphyry Cu-Mo-Au deposits (e.g., Tuwu-Yandong), VMS Cu-Zn-Au deposits (e.g., Huangtupo; Deng et al., 2016), hydrothermal vein Cu (Au) deposits (e.g., Meiling; Mao et al., 2014), and Cu-Ni sulfide deposits (e.g., Baixintan).

The Huangtupo VMS deposit is located on the southern border of the Turpan-Hami Mesozoic-Cenozoic Basin and is tectonically located in the Kalatag area of the Dananhu-Tousuquan island arc zone (Fig. 1C). The Kalatag district consists of an NW-trending Paleozoic anticline in the north part of the Dananhu-Tousuquan island arc belt. The EW-trending Kabei fault and the NWW-trending Kalatag fault represent the northern and southern boundaries, respectively. The strata in this region predominantly comprise Paleozoic mafic to felsic volcanic, volcaniclastic,

and sedimentary rocks intruded by Ordovician to Permian granitic intrusions (Fig. 2A). The Ordovician-Silurian Daliugou Formation (O$_d$), which is the most important ore-bearing stratum, contains three sequences from bottom to top: Unit 1 is composed of deep marine basalts, basaltic andesites, andesites, and volcaniclastic rocks; Unit 2 is dominated by strongly altered tuffaceous breccia, and pyroclastic dacite, with minor siliceous rocks and rhyolite intercalation, and Unit 3 consists chiefly of breccia, rhyolites and dacitic lava with minor interbedded tuffs (Fig. 2A; Deng et al., 2020). These rocks are unconformably overlain and surrounded by volcanic-sedimentary rocks that belong to the Dananhu, Qishan, and Arbasay formations outwards from the Kalatag anticlinal hinge (Fig. 2A). Several Cu-polymetallic deposits, including VMS-type Cu-Zn(Au) deposits (e.g., Huangtupo, Huangtan); hydrothermal vein-type Cu (Au) deposits (e.g., Hongshi, Meiling, Hongshan); porphyry-type Cu deposit (e.g., Yudai); skarn-type Fe-Cu deposit (e.g., Xierqu) and Ni-Cu sulfide deposits (e.g., Yueyawan), were discovered either in the Early Paleozoic or the Late Paleozoic rocks in the northwestern part of the Kalatag district (Fig. 2B; Sun et al., 2019; Deng et al., 2020).

3. Geology of the Huangtupo Cu-Zn (Au) deposit

The Huangtupo Cu-Zn (Au) deposit is located in the southeastern part of the Kalatag district (Fig. 2A) and is structurally controlled by the subsidiary structures of the regional Kalatag fault. The deposit is hosted in the volcanic-volcanic sedimentary sequences of the Late Ordovician - Early Silurian Daliugou Formation (Fig. 2A). The main lithostratigraphic unit, Daliugou Formation, is composed of the lower intermediate-acidic volcaniclastic rock interlayered with basaltic andesite and andesite (Unit 1) and the upper intermediate-acid volcanic rocks (Unit 2–3). The main ore-bearing horizon is overlain by 290–560 m thick Unit 3 volcanic-volcaniclastic rocks, which include andesite, dacite, and dacitic lava (Fig. 3). The disseminated or reticulated Cu mineralization in the footwall mainly developed in the Unit 2 breccia, pyroclastic dacite, and dacitic lavas. In the northeast and southwest of the ore district, the andesitic basalts, dacite, and volcanic breccia are located around the Kalatag granitic intrusions, which consist of quartz diorite, granite porphyry, and granite. In the ore district, NW- and NNW-trending normal faults are widely distributed and control the orebody strike (Fig. 3).

The Huangtupo Cu-Zn (Au) deposit consists of more than 80 orebodies with a total proven reserve of 0.30 Mt Cu (1.49%), 0.28 Mt Zn (3.51%), 7.1 t Au (0.6 g/t) and 281 t Ag (26 g/t) (Deng et al., 2020). It has a typical two-layer structure, with the upper massive sulfide unit of the submarine basin and the lower stockwork mineralization unit. The main Cu-Zn orebodies are characterized by the zoning of metals upward from a deep stockwork mineralized zone (Cu > Zn) to a shallow massive mineralized zone (Zn > Cu) (Fig. 4A, B; Deng et al., 2016). The massive Cu-rich ores are in the core, with banded Zn-rich ores, breccia Zn-rich ores, and pyrite-rich hydrothermal sedimentary siliceous rocks appearing outward from the center (Fig. 4). Some late sulfide veins intersperse massive orebodies (Fig. 4A). The lower part of the massive ore body is a sulfide-silicate stockwork vein system, which is hosted in a series of pyrite-rich volcaniclastic breccias, and amygdaloidal andesitic-basaltic rocks (Fig. 4A). The stockwork is mainly composed of pyrite, chalcopyrite, and small amounts of quartz, sericite, and chlorite. The sparsely disseminated ores are mainly distributed in sericitized rocks at the bottom of the massive ore bodies with relatively abundant copper content. The stockwork ore system extends from the center and comprises scattered sulfide veins in chloritized (sericitized) rocks with a low Cu concentration (0.1%-0.5%). Field observations show that the Huangtupo deposit has four general elemental zonations from the bottom up: Fe ± Cu as a stockwork mineralization zone below the massive orebody; Fe + Cu + Zn + Au + Ag (Cu > Zn) zone in the lower (core) part of the massive ore lens; Fe + Zn + Cu + Au + Ag (Zn > Cu) zone in the middle part of the massive ore lens; and Fe ± (Cu/Zn) zone in the outermost
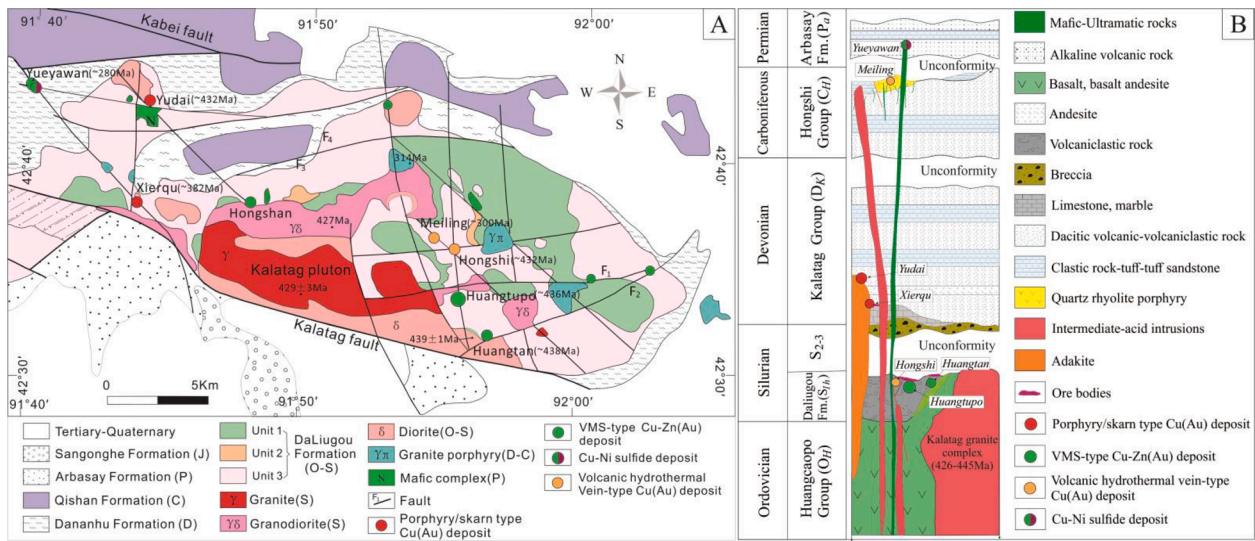
Fig. 2. A. Geological sketch map of the Kalatag district (modified from Mao et al., 2018. Chronological data from Mao et al., 2014, 2018; Deng et al., 2020; Sun et al., 2020); B. Stratigraphic column of Ordovician to Permian strata of the Kalatag district (Xinjiang Geological Survey, unpub. report, 2016).
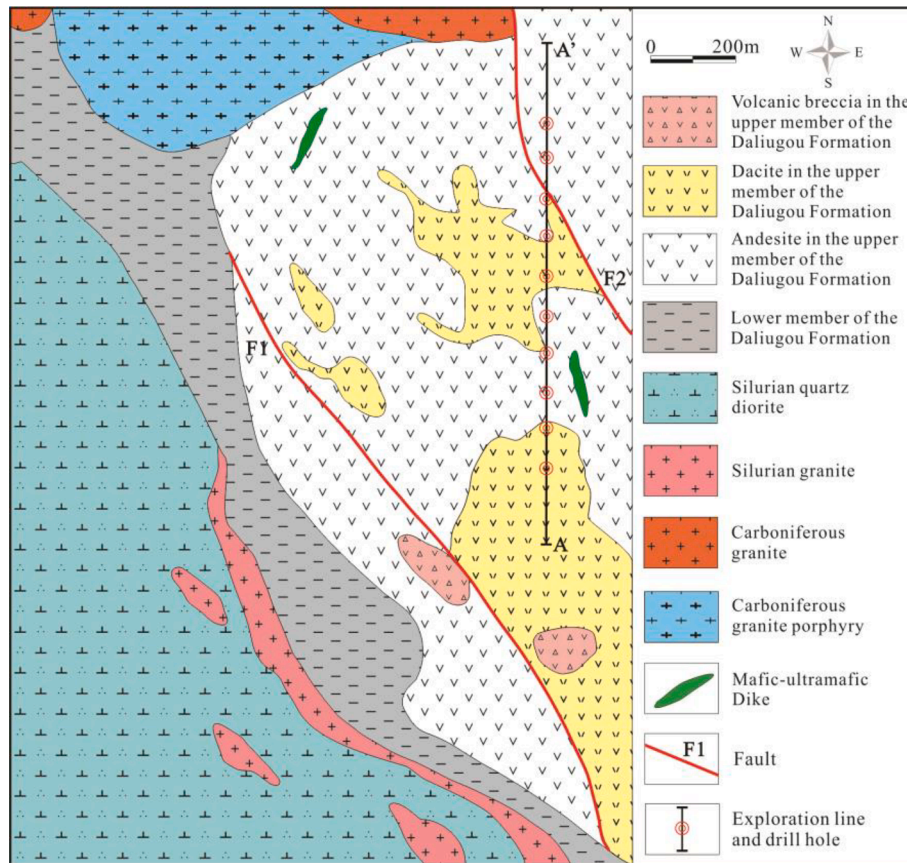
Fig. 3. Simplified geological map of the Huangtupo deposit (modified from XXMCL, 2009).

part of the massive ore lens. Overall, the Zn/Cu ratio decreases with increasing depth (Fig. 4B).

Pyrite, chalcopyrite and sphalerite are the predominant sulfide minerals of the massive ores, associated with minor to trace (<1%) amounts of galena, tetrahedrite, pyrrhotite, bornite, magnetite, hematite and Au-Ag bearing minerals. Chalcopyrite, as an important sulfide, was not highlighted in this study, mainly because of its limited distribution range and the difficulty of generation division. The gangue minerals mainly consist of quartz, pyrite, muscovite, barite, chlorite, and carbonate, with accessory rutile, and apatite. In Huangtupo, pyrite and sphalerite grains show a large variety of textures and morphologies, including brecciated, porous, oscillatory-zoned, inclusion-rich, and subhedral to euhedral pyrite grains. Sulfide minerals occur as disseminations, veinlets or masses with a variety of crosscutting relationships and textures in the alteration zones.

Based on the mineral morphology, texture, and paragenesis, four
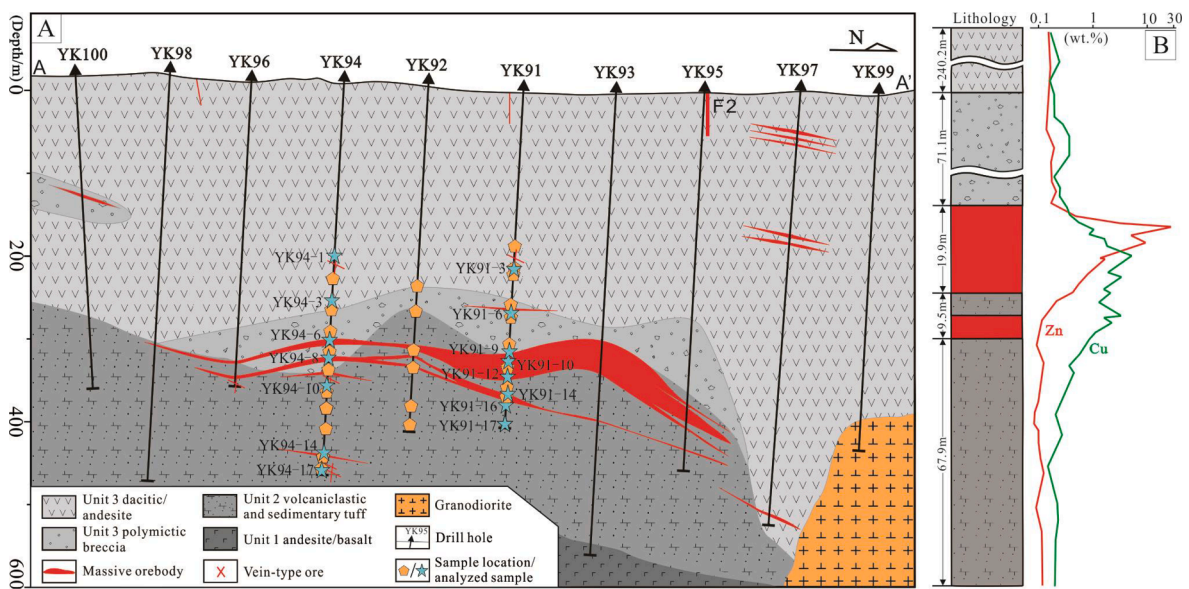
Fig. 4. A. Representative cross sections along exploration line 99 (A-A') showing the occurrence and morphology of the major orebodies at the Huangtupo Cu-Zn(Au) deposit; B. The columnar section of drill hole ZK91 and element content diagram from the Huangtupo deposit.

hydrothermal stages of sulfides are classified (Fig. 5). Disseminated and irregular pyrite aggregates attributed to the preore stage (SI) occur in the basic-intermediate lava, and volcaniclastic breccias within the

Ordovician Daliugou Formation (Fig. 6A). The early ore stage (SII) mainly consists of medium to coarse - grained euhedral pyrite, pyritohedrons, and disseminated sulfide aggregates with small amounts of
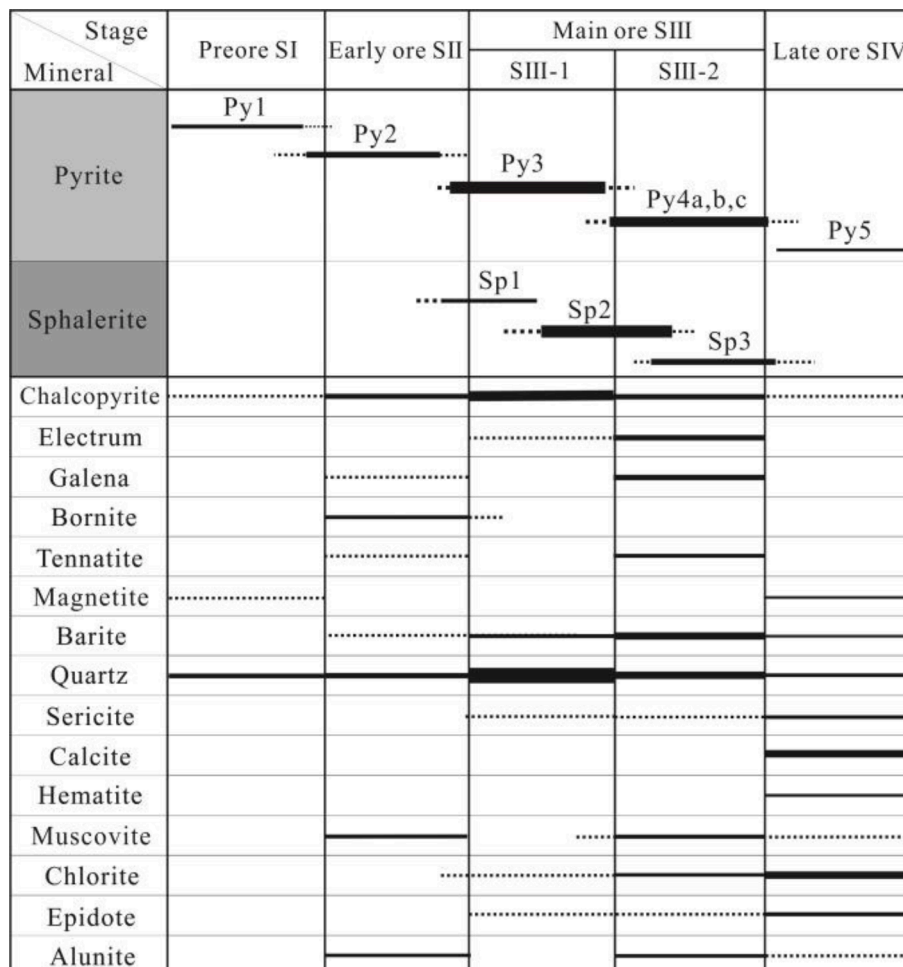
Fig. 5. Paragenetic sequence of Huangtupo Cu-Zn (Au) mineralization interpreted from textures and sulfide geochemistry.
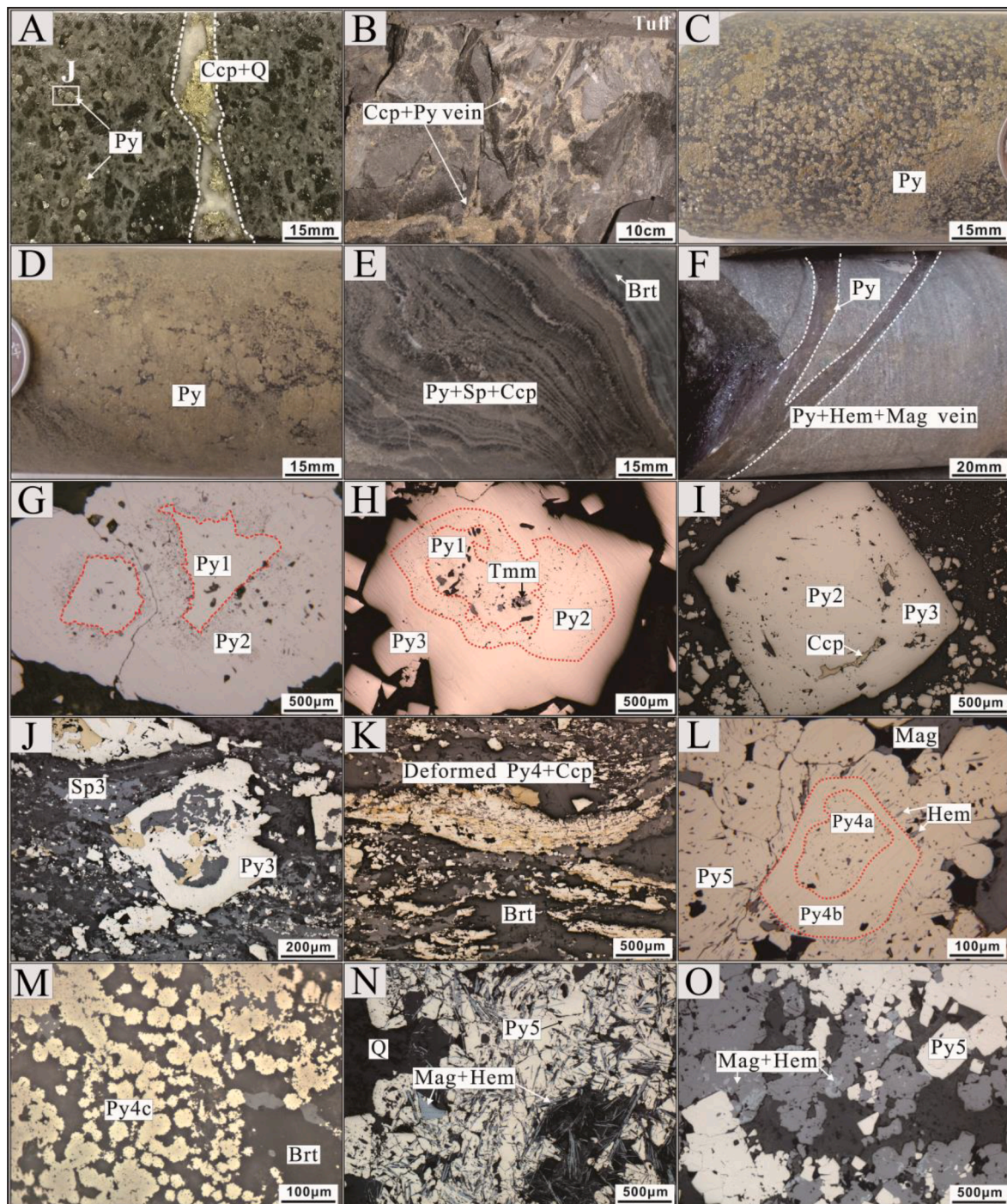
Fig. 6. Photographs of hand specimens (A ~ F) and photomicrographs (plane-polarized reflected light; J ~ O) of pyrite micro-textures from Huangtupo deposit. (A, G). Fine-grained pyrite distributed in the lava at the bottom of an ore body (YK91-17); B. Reticulated pyrite + chalcopyrite in volcanic sedimentary sequences at the bottom of massive orebody; C. Disseminated pyrite in near-ore volcanic sedimentary sequences (YK94-10); D. Pyrite in massive ore bodies (YK111-18); E. Lamellar pyrite, sphalerite and barite (YK111-12); F. Late pyrite + hematite + hematite veins distributed in andesite above massive ore body (YK91-3); G. Py1 in bottom lava (A) is replaced by Py2; H. Multistage pyrite (Py1 ~ 3) in disseminated ores; I. Crystallized pyrite (Py3) in massive ore, coeval with Py2 and chalcopyrite; J. Residual pyrite (Py3) crystal skeleton associated with Sp3; K. Deformed lamellar pyrite (Py4) and chalcopyrite; L. Recrystallized pyrite (Py5) coeval with hematite and magnetite replace early pyrite (Py4a ~ b); M. Framboidal pyrite Py4c; (N, O). Py5 coeval with acicular hematite and magnetite in cap volcanic rocks. Abbreviations: Q, quartz; Brt, barite; Ccp, chalcopyrite; Py, pyrite; Sp, sphalerite; Mag, magnetite; Hem, hematite; Tmm, titanomagnetite.

chalcopyrite, galena, bornite, and silicates (Fig. 6B). The sulfide content of the SIII-1 is dominated by compact massive pyrite - chalcopyrite - sphalerite aggregates that are distributed in the middle and lower part of the massive ore body (Fig. 6C-D). This stage forms the most important Cu-Zn orebodies. The SIII-2 mainly consists of plastic deformed lenticular, laminated pyrite - sphalerite - chalcopyrite assemblage with

abundant galena, barite, silicates, and Au-Ag bearing minerals (Fig. 6E). The late ore stage (SIV) is characterized by widespread fine-grained recrystallized pyrite, carbonate, and hematite-magnetite veinlets in the capping dacite-andesite close to the ore body (Fig. 6F).

Hydrothermal alteration at Huangtupo mainly consists of silicification, pyritization, chloritization, epidotization, and muscovitization

with obvious zonation. Huang et al. (2018) used short-wavelength infrared spectroscopy to divide the deposit into six alteration zones, centered on massive sulfide ore bodies within the quartz + muscovite + pyrite zone, followed upward by the quartz + muscovite + pyrite zone, epidote + chlorite + albite + muscovite + carbonate zone and chlorite + albite + muscovite + carbonate zone; and downward by the chlorite + pyrite ± muscovite zone, and chlorite + quartz + muscovite zone. The volume of the altered volcanic sedimentary rocks in the upper and lower parts of the massive orebody is several times larger than the lenticular massive orebody.

4. Samples and analytical techniques

4.1. Sample selection

Fifty-two representative pyrite and sphalerite samples from different parts of the stockwork and massive mineralized zones were collected at depths of ~450 m to 180 m of the drill holes ZK111, ZK112, ZK94, and ZK91, respectively (e.g., Fig. 4). These samples, representing different stages of mineralization, were selected for in situ compositional and isotopic analyses. Each sample was examined and characterized using transmitted light, reflected light, and scanning electron microscopy (SEM) techniques. A subset of twenty-eight representative pyrite or sphalerite-bearing samples was selected for sulfide compositional (EPMA and LA-ICP-MS) and sulfur isotopic analysis. Thirteen of these samples were collected in the stockwork mineralized zone at regular intervals away from the orebody (>350 m) and fifteen samples were selected from the massive orebody and the overlying volcanic rock (<350 m).

4.2. EPMA and LA-ICP-MS multielement analysis and imaging

4.2.1. Electron Probe Microanalysis (EPMA)

Major element analyses of pyrite and sphalerite were carried out using a JXA-8230 EPMA (Electron Probe Micro-analyzer) equipped with an INCA X-Act spectrometer at the Center for Materials Research and Analysis (CMRA), Wuhan University of Technology (WUT), China. The operating conditions consisted of an acceleration potential of 25 kV, a beam current of 20nA, and a beam diameter of 1–2 μm. Counting times on the peak were 20 s for major elements and 30 s for minor elements. The analytical uncertainty is better than 2%. Average minimum limits of detection and standards for sulfide minerals were summarized in Electronic Appendix Table A3. Detection limits for analyzed elements are typically <300 ppm. EMPA analysis of major elements in pyrite and sphalerite was used for characterization and calibration information for LA-ICP-MS analyses.

4.2.2. Laser ablation-inductively coupled plasma-mass spectrometry (LA-ICP-MS) multielement analysis and imaging

Trace elements in pyrite and sphalerite were analyzed using LA-ICP-MS at the Wuhan SampleSolution Analytical Technology Co., Ltd., Wuhan, China. Laser sampling was performed using a GeolasPro laser ablation system that consists of a COMPexPro 102 ArF excimer laser (wavelength of 193 nm and maximum energy of 200 mJ) and a MicroLas optical system. An Agilent 7700e ICP-MS instrument was used to acquire ion-signal intensities. In this experiment, the laser spot size and frequency were set to 44 μm and 7 Hz, respectively. Elements measured were Si, S, Ti, V, Cr, Mn, Fe, Co, Ni, Cu, Zn, Ga, Ge, As, Se, Mo, Ag, Cd, In, Sn, Sb, Ba, W, Au, Tl, Pb, and Bi. Trace element compositions of minerals were calibrated against various reference materials (NIST 610 and NIST 612). NIST 610 glass was analyzed for each run to monitor the repeatability of the analyses (Electronic Appendix Table A4). The sulfide reference material of MASS-1 (USGS) was used as the unknown sample to ensure the accuracy of the calibration method. Each analysis included a 20–30 s background acquisition followed by 50 s of data acquisition from the sample. Off-line selection and integration of background and

analyzed signals, time-drift correction, and quantitative calibration for trace element analysis were performed using the Excel-based software ICPMSDataCal (Liu et al., 2008). Concentration and detection limit calculations were conducted using the protocol of Longerich et al. (1996).

Samples showing zoning were mapped to define the relationship between different generations of sulfides. The analyses were conducted at the State Key Laboratory of Ore Deposit Geochemistry, Institute of Geochemistry, Chinese Academy of Sciences (IGCAS), Guiyang by using an ASI RESOLution-LR-S155 laser microprobe equipped with a Geo-LasPro 193 nm ArF excimer laser. Line scans were used for trace element maps and carried out using an 8-μm square spot with 12 Hz and a scan speed of 4 μm/s. Signals of both pyrite and sphalerite were calibrated using NIST SRM612 and GSE-1G sulfide reference material, and iron (^{57}Fe) was used as the internal standard (Wilson et al., 2002). Analytical parameters are also provided in Electronic Appendix Table A5. Methods for mapping in pyrite and sphalerite are similar to methods previously reported by Large et al. (2009).

4.3. LA-MC-ICP-MS sulfur isotope analysis

In situ LA-multicollector (MC)-ICP-MS microanalysis was used to determine the δ^{34}S composition of pyrite and sphalerite. Representative polished thin sections analyzed for trace element analysis were repolished and used for in situ S isotope analysis. The analysis was performed on a Neptune Plus LA-MC-ICP-MS (Thermo Fisher Scientific, Bremen, Germany) equipped with a Geolas HD excimer ArF laser ablation system (Coherent, Göttingen, Germany) at the State Key Laboratory of Geological Processes and Mineral Resources (GPMR), China University of Geosciences (Wuhan). The large spot size (44 μm) and slow pulse frequency (2 Hz) were used to avoid the down hole fractionation effect. The laser fluence was kept constant at ~5 J/cm^2. Isotopes ^{32}S and ^{34}S were collected in Faraday cups using static mode. An international sphalerite standard NBS-123 (δ^{34}S$_{V-CDT}$ = +17.8‰ ± 0.2‰) and an in-house pyrite standard named WS-1 (δ^{34}S$_{V-CDT}$ = +1.1‰ ± 0.2‰), consisting of a natural pyrite crystal from the Wenshan polymetallic skarn deposit in Yunnan Province in South China, was used to calibrate the mass bias for sulfur isotopes (Li et al., 2019). The analytical precision for calculating the true sulfur isotope ratio of the unknown sample is approximately ±0.3/mil (2σ).To ensure precision and account for instrument drift, sample measurements were bracketed every four to five analyses by at least one standard measurement. The instrument operating conditions and analytical methods are the same as in Fu et al. (2016).

5. Results

5.1. Paragenesis and petrography of sulfides

The textures of the pyrite and sphalerite ores such as replacement and overgrowth record a series of fluid-flow events. Several generations of sulfides have formed during the hydrothermal history and can be divided into four stages as follows: (i) the preore stage (SI) associated with deep volcanic rock; (ii) the hydrothermal early ore-stage (SII) characterized by veined ore and breccia; (iii) the main ore-stage (SIII) contains massive ore; and (iv) the late ore-stage (SIV) (Fig. 5). Sulfides from the deep sulfide-silicate stockwork orebodies to the shallow lenticular massive orebodies have been grouped into five types based on morphology, paragenesis, and internal texture, including pyrite-1 (Py1) to pyrite-5 (Py5); and sphalerite-1 (Sp1) to sphalerite-3 (Sp3) (Table 1).

Preore stage (SI): The Py1 in the deep breccia and volcanic rocks occurs as subhedral to irregular grains that originally formed as authigenic grains in sub-volcanic rocks or as nodular aggregates carried along with breccias into stockwork zone (Fig. 6A). It rarely preserves euhedral boundaries and usually contains abundant silicate mineral inclusions near the core. Py1 shows intergrowth with minor amounts of

Table 1

Summary of common textures, timing, and sulfur isotopes for pyrite and sphalerite types at the Huangtupo deposit.

Sulfide type	Textures	Timing	Evidences for timing	δ^{34}S (‰)
Py1	Porous subhedral to irregular grains, nodular aggregates	Preore stage (SI)	It contains abundant silicate mineral inclusions and shows similar texture with syndiagenetic pyrite. Overgrown by all later sulfide types.	–2.3 to 2.3; mean = 0.5 (n = 12)
Py2	Medium to fine-grained, clear euhedral to subhedral aggregates with Py1 core	Early ore-stage (SII)	Distributed in the deep stockwork ores; overgrows Py1	0.0 to 3.1; mean = 1.0 (n = 15)
Sp1	Anhedral, metasomatic residual grains	Main ore-stage (SIII-1)	Red to dark red; overgrown by later sphalerite types; Disseminations in the laminated siliceous tuffs of the orebody footwall or the massive ore	1.2 to 3.1; mean = 2.7 (n = 8)
Py3	Corase-grained, clear euhedral to subhedral aggregates with earlier pyrite core	Main ore-stage (SIII-1)	Occur at the bottom of massive Cu orebody; overgrows Py2	–0.3 to 2.2; mean = 1.6 (n = 10)
Sp2	Corase-grained, euhedral aggregates	Main ore-stage (SIII-1)	Overgrows Sp1 and surrounds Py3	1.2 to 3.0; mean = 2.2 (n = 7)
Py4a	Corroded porous aggregates with abundant sulfide microinclusions	Main ore-stage (SIII-2)	Distributed on the top of deformed massive Zn-Cu orebody and veined ores; Replacement of early massive sulfides, including Py3	2.5 to 5.2; mean = 4.2 (n = 5)
Py4b	Clear euhedral grains with Py4a core	Main ore-stage (SIII-2)	Distributed on the top of deformed massive Zn-Cu orebody and veined ores; overgrows Py4a	1.7 to 4.9; mean = 3.5 (n = 6)
Py4c	Fine-grained framboids	Main ore-stage (SIII-2)	Distributed on the top of deformed massive Zn-Cu orebody and veined ores; coexists with recrystallized sphalerite (Sp3)	3.5 to 5.8; mean = 4.0 (n = 6)
Sp3	Recrystallized, plate-like aggregates	Main ore-stage (SIII-2)	Distributed on the top of deformed massive Zn-Cu orebody and veined ores; Overgrows Sp1 ~ Sp2 and coexists with Py4	–3.7 to 1.8; mean = –0.1 (n = 24)
Py5	Medium to fine-grained euhedra	Late ore-stage (SIV)	Distributed in late sulfide veins in the upper volcanic rocks of the massive orebody; coexists with acicular hematite and magnetite	0.4 to 2.8; mean = 1.6 (n = 9)

chalcopyrite and magnetite in the interstices of these grains (Fig. 6G-H). The size of Py1 is 10 μm to 3 mm in diameter. Most of Py1 exhibits core–edge texture, where Py2 overgrows Py1 (Fig. 6G-H).

Early ore-stage (SII): The SII consists of abundant medium to fine-grained disseminated pyrite (Py2) with minor chalcopyrite and sphalerite. These sulfides are mainly distributed in the stockwork ores (Cu-rich zone) broadly concordant with a fluid passageway in the deep breccias (Fig. 6B). This pyrite generation (Py2) is euhedral to subhedral and has a size of 50 μm to 5 mm in diameter. It locally overgrows porous

cores of diagenetic Py1 with minor chalcopyrite and quartz inclusions (Fig. 6G-H). Py2 is most abundant in the vein-hosted zone (Fig. 6B).

Main ore-stage (SIII): The SIII consists of abundant hydrothermal sulfides including Py3 to Py4, Sp1 to Sp3, and some base metal sulfides. Most pyrite ores were formed during this period. It can be divided into an early Cu-Fe-dominated massive sulfide stage and a late Zn-Cu-dominated deformed sulfide stage. In the SIII-1, euhedral to subhedral Py3 is mainly distributed in the siliceous volcanic rock of the orebody footwall and the Cu (Fe)-rich zone at the base of the massive orebody (Fig. 6C-D). This type of pyrite is generally well crystalline with large grains between 100 μm and 10 mm and is mostly disseminated in tuffaceous breccia and massive in ores (Fig. 6C-D, H-I). These grains are devoid of petrogenic mineral inclusions and locally overgrow earlier Py2 as euhedral thin rims (50 μm –1 mm thickness) (Fig. 6H-I).

In addition, Py3 is commonly coeval with early chalcopyrite and sphalerite in massive ores. Sphalerite at this stage appears as lamellar, massive ore (Fig. 7A-C), and consists of two main types. Type 1 is red sphalerite (Sp1) (Fig. 7D-E, H), but it is mostly replaced by type 2 yellow sphalerite (Sp2) which is the most abundant sphalerite in the ore (Fig. 7D-E, I). Sp2 mostly overgrows on Sp1 as euhedral or subhedral grains and is also intergrown Py3. The lower tuffaceous breccia of the massive orebody contains abundant structurally intact granular sphalerite, which preserves the metasomatic relationship of the three-stage sphalerite (Fig. 7A, E).

The SIII-2 is composed of three sub-generational pyrites (Py4a ~ c), including porous and framboidal, associated with the Zn-rich part of the massive ore (Fig. 6E). Py4a at this stage commonly contains early mineral inclusions, including visible chalcopyrite, sphalerite, and silicate inclusions (Fig. 6K-L). Py4b grows at the periphery of Py4a and has a cleaner texture with fewer inclusions (Fig. 6L). Furthermore, Py4b is overgrown by porous pyrite (Py4c), which is coeval with recrystallized sphalerite (Sp3) containing plentiful electrum particles (Fig. 7F-G and 8A). Framboidal Py4c aggregates are commonly abundant in the deformed layered ore bodies at the top of the massive ore bodies or occur as disseminations in the microcrystalline quartz-pyrite cement and silicified tuff (Fig. 6E, M). In the SIII-2 stage, the mineral assemblage is diverse including minerals such as chalcopyrite, tetrahedrite, galena, and silver-bearing minerals (Fig. 9).

Late ore-stage (SIV): Recrystallized Py5 is defined as the latest pyrite type, which commonly coexists with acicular hematite and magnetite in late sulfide veins in the upper volcanic rocks of the orebody (Fig. 6F). It forms almost perfectly euhedral crystals with varying particle sizes (0.2–2 mm) and acts as recrystallized rims on some of the other types of pyrite (Fig. 6N-O). The recrystallized Py5 rim appears to be common around the residual Py4 (Fig. 6L) and other types of sulfides in ores, but is absent in pyrite from the center of the massive sulfide zones. The ore at this stage is subjected to late tectonic activity and fluid modification, resulting in plastic or brittle deformation structures and significant mineral recrystallization. The paragenetic sequence of Huangtupo Cu-Zn (Au) mineralization is summarized in Fig. 5.

5.2. Trace element distribution and associations in pyrite and sphalerite

Trace elements compositions of various sulfides determined by LA-ICP-MS are given in Electronic Appendix Tables A1~A2 and summarized in Tables 2~3. Representative ablation profiles for different generations of pyrite and sphalerite are illustrated in Figs. 14-16. It is worth noting that the analysis was carried out as far as possible in inclusion-free pyrite or sphalerite areas, but it was not possible to completely avoid inclusions that are below the sample surface.

Composition of Py1: Subhedral to anhedral Py1 in the deep basaltic rocks shows generally high concentrations of As, Au, Co, Cu, Mn, Ni, Pb, Se, Ti, and V (Fig. 10). The wide range of values for Zn, Cu, and Pb are likely due to the abundant micro-inclusions of sphalerite, chalcopyrite, and galena (Fig. 10). Some Py1 grains are syngenetic with ilmenite and titanomagnetite inclusions, which could explain the high Ti content. The
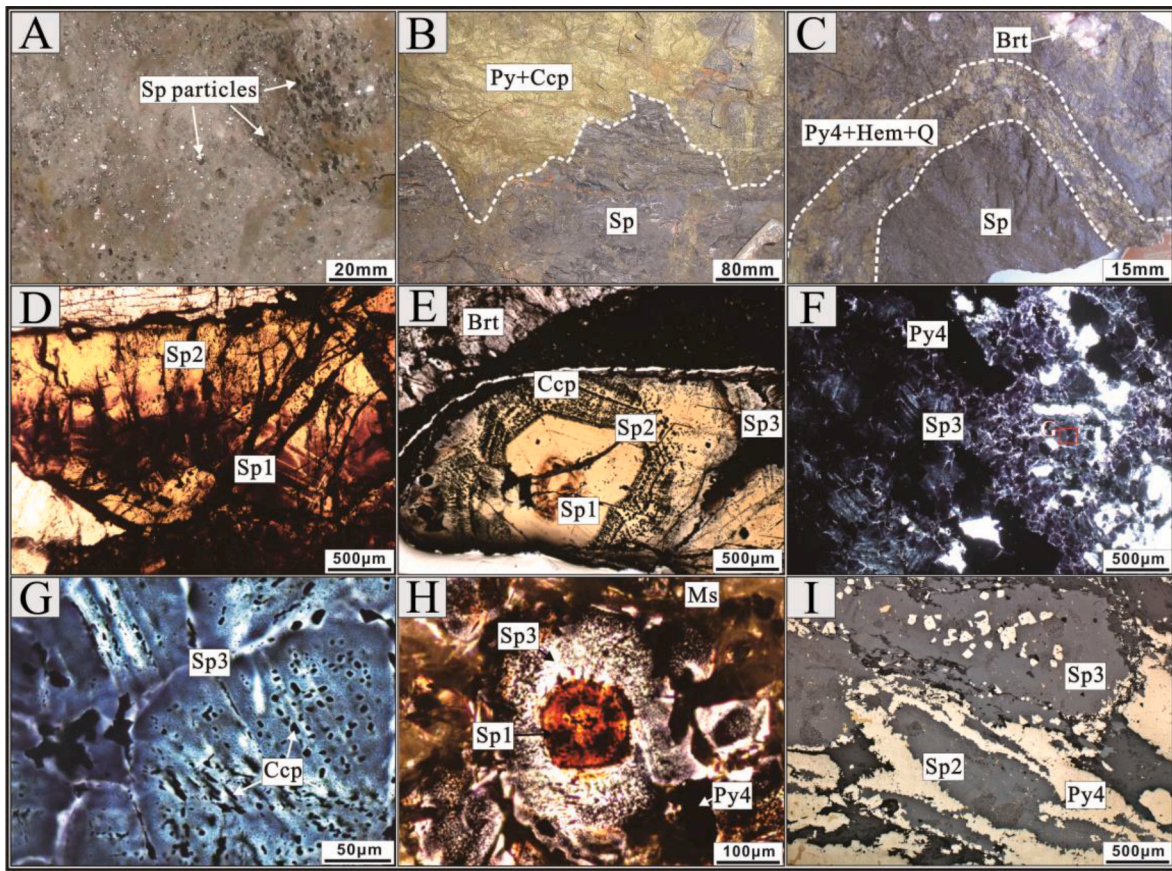
Fig. 7. Photographs of ores (A-C) and photomicrographs (D-I; plane-polarized reflected and transmitted-light) of representative sphalerite micro-textures from Huangtupo deposit. A. Disseminated sphalerite grains in the tuff at the bottom of the massive ore body; B. Massive chalcopyrite, pyrite and sphalerite ores; C. Recrystallised pyrite-magnetite vein cut through sphalerite ores; D. Red Sp1 is replaced by yellow Sp2 (YK91-14); E. Transition from residual Sp1 at the core to crystalline Sp2 ~ 3 at the edge (YK91-16); (F, G). Recrystallised Sp3, exsolved chalcopyrite distributed along cleavage (YK91-9); H. Sp1 is replaced by Sp3 directly (YK111-13); I. Sp2 is replaced by Py4, which is coeval with Sp3 (YK111-12). Abbreviations: Brt, barite; Ccp, chalcopyrite; Py, pyrite; Sp, sphalerite; Ms, muscovite; Hem, hematite.
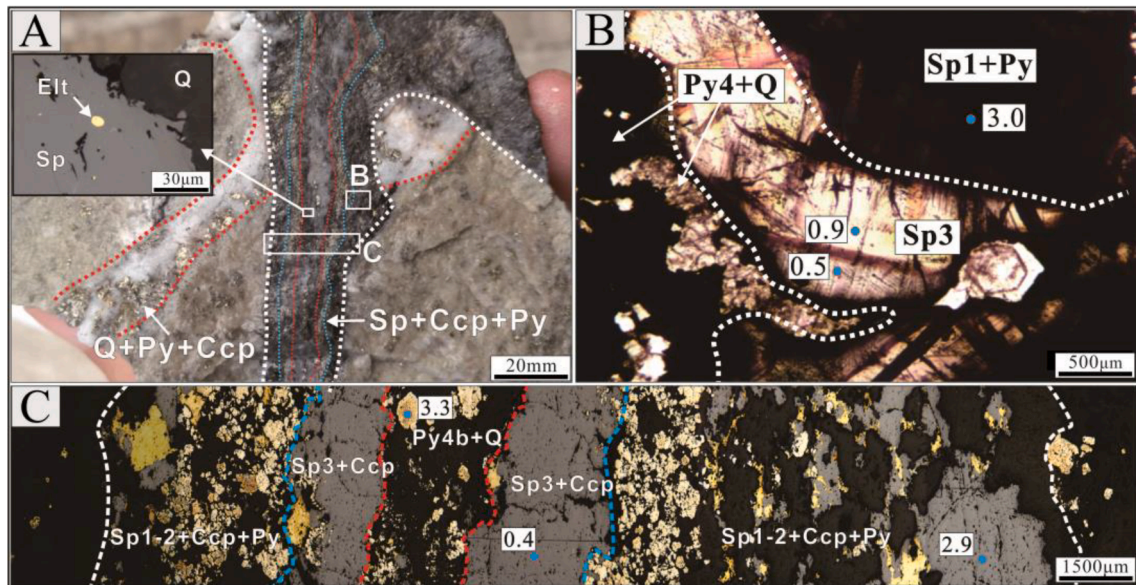
Fig.8. Photographs of electrum-bearing SIII-2 quartz-sulfide vein in the siliceous tuff (sample HTP-10), exhibiting the distribution of pyrite and sphalerite. A. Hand specimen; B. Transmitted-light photograph; C. Reflected-light image. Blue circle spots represent in situ sulfur isotope positions. Numerical labels represent $\delta^{34}S$ values.
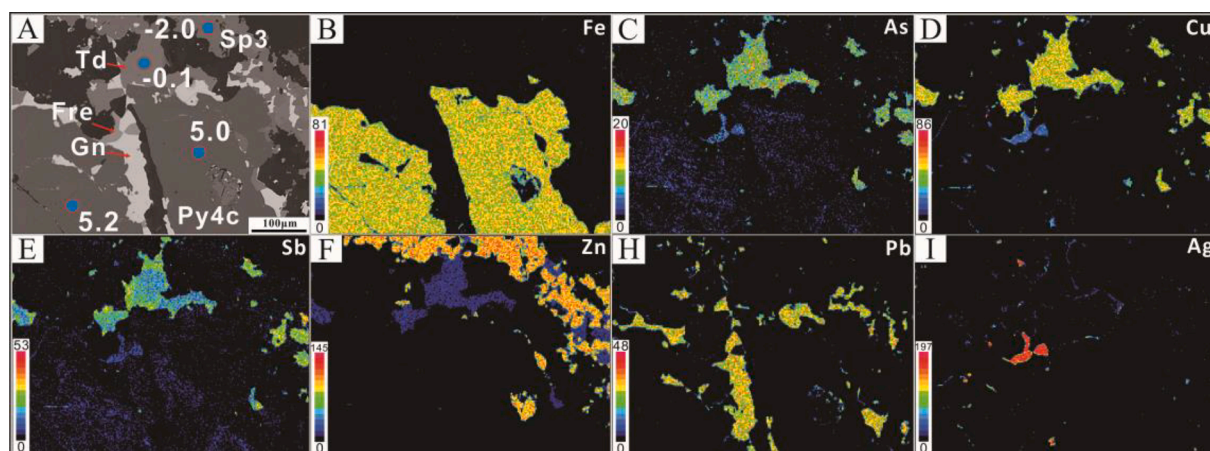
Fig. 9. Backscattered electron images (A) and corresponding X-ray elemental maps (B-I) of selected pyrite (Py4b ~ c) and sphalerite (Sp3) assemblages (sample YK111-12). Blue circle spots represent in situ sulfur isotope positions. Numerical labels represent δ^{34}S values. Abbreviations: Py, pyrite; Sp, sphalerite; Td, tetrahedrite; Gn, galena; Fre, freibergite.

gold content in Py1 varies from 0.08 to 7.10 ppm with a mean of 2.68 ppm, while arsenic varies from 1331 to 33237 ppm (mean = 8394 ppm, s.d. = 2.07, n = 20). Cobalt and Ni concentrations in Py1 display variations up to four orders of magnitude, with concentrations from 110 to 4586 ppm for Co and 3 to 18655 ppm for Ni. LA-ICP-MS elemental maps show that Py1 has a complex distribution for most elements compared to the enveloping nonporous Py2 aggregates, especially the elements mentioned above (Fig. 14). This phenomenon may be attributed to the abundant inclusions in Py1.

Composition of Py2: Fine-grained disseminated Py2 shows generally low concentrations of most elements compared to diagenetic Py1 (Fig. 10). The contents of As, Zn, Cu, Tl, and Pb in Py2 are the lowest among pyrite of each stage in Huangtupo (Fig. 10). About 90% of Py2 analyses have a relatively low gold content, with values varying from below the detection limit to 0.83 ppm and a mean of 0.53 ppm (n = 20). The presence of a few extreme values of Au and As may represent the existence of arsenopyrite micro-inclusions. LA-ICP-MS mapping results show that Py2 overgrows earlier cores of Py1 and has no clear growth zoning as most elements are depleted (Fig. 14).

Composition of Py3: LA-ICP-MS data shows that the euhedral Py3 in the massive ores (Cu > Zn zone) has similar element distribution characteristics to Py2 (Fig. 10). It has low concentrations of most elements. For example, Py3 contains low concentrations of both Au and As with a mean of 0.51 ppm (s.d. = 0.71, n = 21) and 201 ppm (s.d. = 262, n = 21), respectively. In the box plots it can be seen that the Py3 aggregates are slightly enriched in Cu, Zn, Sb, Pb, and As except for Co, and Se, compared to Py2 (Fig. 10).

Composition of Py4: Compared to earlier generations of pyrite, the laminar deformed porous Py4 in the upper part of the massive sulfide orebody is enriched in most trace elements such as Ag, As, Au, Cu, Mn, Sb, Tl, and Zn, but relatively depleted in Co, Ni, and Se. Py4, specifically, can be subdivided into three sub-generations: porous Py4a is enriched in Au, Bi, Cu, Sb, In, and Zn, while crystalline Py4b is relatively enriched in As, Au, and Co, and framboidal Py4c is relatively enriched in Ag, As, Au, Cu, Mn, Pb, Tl, and Zn (Fig. 10; Table 2).

Anhedral Py4a grains are noticeably more enriched in Cu, Zn, and Au with some tiny (0.5 ~ 5 µm) inclusions randomly distributed across the grain. The majority of spot analyses for Py4a exhibit Cu, Zn, and Au contents ranging from 74 to 18765 ppm (mean 5854 ppm, s.d. = 6276, n = 18), 3–15641 ppm (mean 2613 ppm, s.d. = 4380, n = 18), and < 0.01–37.59 ppm (mean 6.21 ppm, s.d. = 8.82, n = 18), respectively. Py4b lacks abundant mineral inclusions, but most analyses still show a Au content between 0.08 and 7.73 (mean 2.16 ppm, s.d. = 2.78, n = 15) and As content varies from 487 to 23,034 (mean 8847 ppm, s.d. = 7442, n = 15). Framboidal Py4c mostly exhibits relative enrichment in As

(mean 33401 ppm, s.d. = 37376, n = 23), Au (mean 17.36 ppm, s.d. = 22.30, n = 23), and Zn (mean 2412 ppm, s.d. = 2977, n = 23). Fig. 16 illustrates LA-ICP-MS elemental maps of a multi-stage pyrite (Py4a ~ b and Py5) grain collected from a metasomatic deformed ore containing irregularly distributed sulfide inclusions.

Composition of Py5: This generation of pyrite (Py5) has the lowest concentrations of most elements but is relatively enriched in Co, Ni, and Se compared with Py2-4 (Fig. 10). Approximately 90% of the Py5 samples analyzed were coeval with hematite and magnetite (Fig. 6L, N), and had the lowest gold content with values between <0.01 and 3.76 ppm and a mean value of 0.34 ppm (s.d. = 0.75, n = 26; Fig. 10). The disparity of trace element concentrations between Py4a-b and Py5 is clearly displayed in the trace element maps of a coarse-grained Py4a-b overgrown by Py5 zoning (Fig. 16). The Py5 is relatively enriched in Co, Ni, and minor Bi compared to the inner Py4, which contains most of the trace elements. In addition, the Co-Ni binary diagram shows that the Co and Ni contents of pyrite generations in the stockwork zone (Py1 ~ 2 and Py5) are significantly higher than in pyrite from the massive sulfide zone (Py3 ~ 4), which may be a good indicator to distinguish stockwork and massive sulfide ores (Fig. 11F; Marques et al., 2006).

Composition of Sp1-3: Different generations of sphalerite exhibit obvious differences in color and trace element content. In deep veined ore zones, sphalerite appears as euhedral-subhedral grains (Sp1 ~ 2) with distinct boundaries toward late hydrothermal minerals, such as pyrite and sphalerite (Sp2 ~ 3). The early red Sp1, which is coeval with Py3, is relatively deficient in In and Mn, but enriched in Ag, As, Fe, Ge, Pb, and Sb compared to Sp2 (Table 3). Some Sp1 grains show chemical heterogeneity and exhibit clear traces of replacement by Sp2 with oscillatory ring bands (Fig. 7E). Yellow Sp2 is the most abundant type of sphalerite, which is syngenetic with Py3 and Py4a. It is more transparent than the early sphalerite and rich in chalcopyrite inclusions, but relatively deficient in trace elements such as Ag, As, Au, Pb, and Sb (Fig. 12). Veinlets of colorless to light purple Sp3 commonly occur in massive or lamellar ore bodies and are associated with barite and Au-rich pyrite (Py4). It shows low concentrations for all trace elements, but In. LA-ICP-MS elemental maps (Fig. 15) show that Sp3, which is syngeneic with barite, overgrows earlier cores of Sp1 and contains low contents of most elements. As shown in X-ray elemental maps (Fig. 9), Sp3 is associated with a variety of coeval minerals including galena, tetrahedrite, various Au-Ag bearing minerals, and silicate.

5.3. Sulfur isotope compositions

All sulfur isotope compositions measured by in situ LA-MC-ICP-MS are shown in Table 4 and graphically illustrated in Figs. 17-19. These

Table 2
Laser ablation-inductively coupled plasma-mass spectrometry (LA-ICP-MS) analyses of pyrite from within and outside the ore zone of the Huangtupo Cu-Zn(Au) deposit (data in ppm).

	Ti	V	Cr	Mn	Co	Ni	Cu	Zn	As	Se	Mo	Ag	Cd	Sn	Sb	Ba	W	Au	Tl	Bi	Pb
Py1(n = 20)																					
Avg	440.28	9.79	4.33	25.54	2042.62	3124.76	635.35	145.34	8394.70	1014.44	2.06	8.92	2.41	2.21	11.89	12.82	2.02	2.68	0.74	16.12	865.60
S.D.	720.46	11.62	5.10	27.11	1345.52	4769.33	825.34	178.14	8190.79	1675.23	4.90	13.78	8.63	2.33	15.03	34.80	2.98	2.07	1.44	13.63	1232.14
Max	3159.29	37.65	18.11	86.88	4586.56	18655.71	3303.56	757.33	33237.27	6862.18	22.86	54.38	39.95	9.13	52.09	160.53	12.41	7.10	6.50	46.07	3856.91
Min	6.78	b.d.l	b.d.l	2.16	110.58	3.27	23.97	5.12	1331.62	b.d.l	b.d.l	b.d.l	b.d.l	b.d.l	b.d.l	b.d.l	b.d.l	b.d.l	b.d.l	0.06	0.42
Median	71.20	3.64	2.46	14.96	2376.20	370.03	240.15	67.11	4287.48	432.09	0.49	3.83	0.30	1.75	7.35	2.15	1.05	1.28	0.15	14.10	139.91
Py2(n = 24)																					
Avg	16.90	0.28	2.24	2.31	241.54	14.41	92.36	21.97	56.65	274.20	0.09	10.72	0.11	0.51	0.50	0.21	0.02	0.53	0.03	3.07	16.80
S.D.	18.86	0.66	4.06	4.64	325.67	23.26	102.21	0.00	120.02	343.12	0.22	16.35	0.19	1.09	1.33	0.39	0.03	0.94	0.06	9.13	38.55
Max	59.89	2.99	16.42	19.15	997.63	82.37	319.74	200.25	476.09	407.23	1.07	63.34	0.91	5.11	6.61	1.83	0.07	4.36	0.24	45.48	175.22
Min	4.89	b.d.l	b.d.l	b.d.l	b.d.l	b.d.l	0.20	0.87	b.d.l	b.d.l	b.d.l	b.d.l	b.d.l	b.d.l	b.d.l	b.d.l	b.d.l	b.d.l	b.d.l	b.d.l	0.03
Median	6.55	0.04	0.47	0.39	45.89	3.03	55.51	0.00	9.20	151.60	0.02	0.93	0.03	0.14	0.06	0.06	0.00	0.18	0.00	0.35	1.56
Py3(n = 21)																					
Avg	15.72	0.72	1.88	42.57	37.82	19.54	166.40	86.05	201.05	260.93	4.98	10.71	0.30	0.90	19.06	0.39	0.66	0.51	7.37	24.15	148.15
S.D.	14.22	1.33	2.74	86.67	52.63	37.80	223.04	144.28	262.05	404.01	16.71	17.08	0.92	1.51	26.02	0.84	1.55	0.71	17.76	63.08	233.49
Max	46.56	4.96	8.79	355.52	160.10	143.06	777.62	488.18	689.68	1455.75	79.20	63.53	4.35	6.00	93.92	3.74	6.83	1.92	50.72	252.24	868.82
Min	5.13	b.d.l	b.d.l	b.d.l	b.d.l	b.d.l	1.20	b.d.l	b.d.l	b.d.l	b.d.l	b.d.l	b.d.l	b.d.l	b.d.l	b.d.l	b.d.l	b.d.l	b.d.l	b.d.l	b.d.l
Median	8.41	0.05	0.46	3.91	8.83	1.49	37.34	34.37	25.89	65.94	0.15	1.85	0.00	0.22	0.22	0.06	0.01	0.06	0.02	0.46	23.13
Py4a(n = 18)																					
Avg	24.54	0.67	5.77	79.46	44.77	43.85	5854.22	2613.03	11936.96	93.94	8.71	129.21	19.62	1.24	1093.02	20.01	0.11	6.21	70.08	16.70	3311.77
S.D.	20.63	1.11	6.58	103.46	81.36	60.20	6276.04	4380.78	17445.94	183.41	16.19	242.12	43.50	2.18	2191.85	46.50	0.12	8.82	117.47	19.87	11971.50
Max	57.74	4.23	19.33	395.29	294.32	261.26	18765.80	15641.23	78015.17	772.47	60.09	1043.82	164.77	9.20	9315.90	168.92	0.43	37.59	376.55	84.07	52559.14
Min	5.75	b.d.l	b.d.l	0.43	b.d.l	b.d.l	74.62	3.43	13.18	b.d.l	b.d.l	0.06	b.d.l	b.d.l	b.d.l	b.d.l	b.d.l	0.46	0.02	b.d.l	0.39
Median	8.78	0.12	2.88	31.31	5.21	30.24	2263.71	242.69	7485.24	35.77	2.20	53.36	0.39	0.39	66.47	1.77	0.07	3.27	0.14	12.90	67.13
Py4b(n = 15)																					
Avg	10.42	1.32	1.50	93.76	30.27	15.06	374.79	38.85	8847.28	53.76	4.27	38.35	0.21	0.21	602.19	2.05	0.39	2.16	98.19	17.16	411.28
S.D.	12.93	2.11	1.29	98.29	46.56	30.42	579.75	39.59	7442.34	79.39	5.62	53.46	0.45	0.18	1121.53	2.99	0.68	2.78	175.34	38.32	534.88
Max	60.16	7.80	4.77	298.23	155.54	119.11	2394.26	115.54	23034.68	326.65	18.54	196.17	1.89	0.68	4158.01	10.27	2.79	7.73	656.53	157.50	2026.77
Min	4.53	b.d.l	b.d.l	b.d.l	b.d.l	b.d.l	6.53	3.13	487.23	b.d.l	b.d.l	b.d.l	b.d.l	b.d.l	b.d.l	0.05	b.d.l	0.08	b.d.l	b.d.l	0.37
Median	7.21	0.31	1.17	59.17	5.76	1.32	205.42	21.24	7578.25	19.84	2.00	21.45	0.08	0.19	68.03	0.40	0.12	0.72	19.74	0.33	162.13
Py4c(n = 23)																					
Avg	25.95	2.42	6.00	1913.81	46.55	36.55	5327.43	2412.21	33401.71	227.05	48.43	401.40	20.72	0.96	6706.16	10.70	1.34	17.36	507.26	10.98	3516.31
S.D.	21.38	3.59	4.62	1738.64	94.25	57.43	5873.72	2977.67	37376.64	610.70	64.85	370.01	67.86	1.03	10237.51	31.69	2.81	22.30	983.01	32.56	5423.02
Max	97.69	14.63	13.75	6416.98	420.06	257.96	21512.49	10721.22	104185.70	2877.88	193.99	1242.96	334.49	3.25	31789.14	157.93	10.94	60.28	4766.33	131.92	24166.27
Min	5.07	0.10	0.13	4.95	b.d.l	b.d.l	452.12	3.89	325.57	6.88	b.d.l	16.54	b.d.l	b.d.l	22.54	0.20	b.d.l	0.79	0.78	b.d.l	108.85
Median	25.93	0.98	4.14	1244.92	0.40	15.83	2137.80	1183.26	14960.18	6.88	16.36	260.12	2.25	0.69	712.16	1.94	0.08	4.45	140.74	0.06	1990.22
Py5(n = 26)																					
Avg	31.49	1.93	5.01	8.38	1355.10	301.90	45.33	79.44	93.78	1885.49	2.92	1.97	0.53	0.91	1.37	1.53	2.07	0.34	0.29	12.22	65.33
S.D.	18.08	2.47	5.93	12.97	1110.18	436.81	59.16	131.25	143.12	2907.93	7.01	3.25	0.67	1.34	2.59	1.72	5.72	0.75	0.56	23.73	159.19
Max	63.63	8.79	25.58	52.76	3824.74	1625.81	312.86	528.26	557.12	10624.83	34.47	14.58	1.92	4.83	9.89	6.12	30.15	3.76	2.17	122.20	633.34
Min	4.54	b.d.l	b.d.l	b.d.l	22.66	0.74	7.93	1.01	5.54	b.d.l	b.d.l	b.d.l	b.d.l	b.d.l	b.d.l	b.d.l	b.d.l	b.d.l	b.d.l	b.d.l	0.08
Median	33.00	0.36	3.14	4.00	1001.70	61.85	28.10	37.86	22.93	771.49	0.36	0.46	0.13	0.33	0.38	0.97	0.46	0.08	0.03	3.83	6.83

S.D. = standard deviation, b.d.l = below detection limit.

Table 3
Laser ablation-inductively coupled plasma-mass spectrometry (LA-ICP-MS) analyses of sphalerite from within and outside the massive ore zone of the Huangtupo Cu-Zn(Au) deposit (data in ppm).

	Ti	Cr	Mn	Fe	Cu	Ga	Ge	As	Se	Mo	Ag	Cd	In	Sn	Sb	Ba	Au	Pb
Sp1(n = 21)																		
Avg	2.46	4.69	900.74	16703.45	2585.95	40.05	18.57	94.08	21.26	98.94	181.99	1705.94	1.80	0.98	718.78	0.11	0.20	67.58
S.D.	0.54	7.93	967.77	5536.30	3035.07	79.44	28.85	84.30	31.18	146.42	230.51	226.84	3.60	0.51	502.46	0.20	0.25	97.27
Max	3.64	27.56	2559.46	33576.63	13337.02	327.25	136.46	311.09	86.48	564.55	817.17	2204.21	16.18	2.12	1834.95	0.84	1.23	382.99
Min	1.52	b.d.l	12.80	9394.21	378.82	0.23	0.08	b.d.l	b.d.l	0.16	4.34	1413.72	b.d.l	0.41	93.13	b.d.l	0.04	0.02
Median	2.29	1.15	266.97	16191.90	1390.99	4.17	13.38	52.59	0.00	26.08	82.15	1700.50	0.51	0.88	512.58	0.06	0.13	13.96
Sp2(n = 17)																		
Avg	2.57	1.05	1787.26	7421.61	1859.96	24.57	3.92	2.19	38.20	17.31	7.00	1561.95	3.47	0.96	1.61	1.61	0.07	4.08
S.D.	1.14	1.20	1072.57	4990.71	2703.00	32.38	5.22	1.54	47.98	64.32	4.25	107.22	4.63	0.84	1.87	1.87	0.12	4.66
Max	6.91	5.32	3012.05	16978.52	8846.74	131.85	21.94	5.75	181.84	274.49	18.08	1742.19	17.74	4.04	5.02	6.93	0.51	18.93
Min	1.68	0.37	81.26	1250.38	12.13	1.10	b.d.l	b.d.l	b.d.l	b.d.l	1.42	1408.14	b.d.l	0.49	0.20	0.04	b.d.l	b.d.l
Median	2.44	0.82	2289.85	7454.33	556.50	10.59	1.29	2.20	22.39	0.03	6.94	1578.63	1.23	0.75	0.96	0.00	0.04	3.65
Sp3(n = 49)																		
Avg	2.84	10.31	147.66	5865.87	3364.56	20.38	1.49	10.70	91.01	1.93	32.22	1368.85	15.26	0.96	5.75	5.75	0.14	21.060
S.D.	2.25	23.08	174.41	4880.38	2986.19	24.32	3.75	27.82	190.64	3.63	36.02	434.80	19.16	0.32	9.84	9.84	0.19	19.962
Max	17.61	113.02	736.08	20417.66	14766.61	101.39	23.49	155.10	1010.67	12.96	226.70	2294.31	37.90	2.28	40.03	40.03	1.09	87.403
Min	1.19	0.31	3.11	2013.71	76.62	0.31	b.d.l	b.d.l	b.d.l	0.00	2.51	552.12	b.d.l	0.46	b.d.l	b.d.l	b.d.l	1.014
Median	2.53	1.73	77.33	4475.65	2568.17	7.61	0.41	3.89	17.43	0.10	23.66	1294.75	8.21	0.95	2.45	0.06	0.10	15.489

S.D. = standard deviation, b.d.l = below detection limit.

data reveal the variation of sulfur isotopes between different generations of pyrite (Py1-5) and sphalerite (Sp1-3).

δ34S of pyrite: Py1 formed during diagenesis typically has δ^{34}S values ranging from −2.3 to 2.3‰ (mean = 0.5 ‰, s.d. = 1.38, n = 12; Fig. 17). The δ^{34}S values of disseminated euhedral Py2 aggregates are similar to the earlier diagenetic Py1, with a range of 0.0 to 3.1‰ (mean = 1.0 ‰, s. d. = 0.87, n = 15). Ten spot analyses on coarse-grained euhedral Py3 grains show a variation in δ^{34}S values from −0.3 to 2.2‰ with a mean of 1.6 ‰ (s.d. = 0.71). Five-spot analyses on porous metal inclusions-enriched Py4a microcrystal aggregates are slightly high compared to the earlier pyrite generations, with a range of 2.5 to 5.2‰ (mean = 4.2 ‰, s.d. = 1.11, n = 5). Clean crystalline Py4b shows a similar range of δ^{34}S, from 1.7 to 4.9‰ with a mean of 3.5 ‰ (s.d. = 1.17, n = 6). Similarly, framboidal and microcrystalline Py4c has a relatively uniform range of δ^{34}S compositions, ranging from 3.5 to 5.8 ‰ (mean = 4.0 ‰, s. d. = 0.95, n = 6; Fig. 17). Compared with the sulfur isotopic range of Cu-Au-rich Py4, the late recrystallized Py5 has lower δ^{34}S values, ranging from 0.4 to 2.8‰ (mean = 1.6 ‰, s.d. = 1.38, n = 9).

δ34S of sphalerite: Sulfur isotope analyses of individual sphalerite display a gradual depletion in δ^{34}S from the core to the rim (Fig. 18). Sp1 crystals have the most positive δ^{34}S values of the entire series. The δ^{34}S of subsequent generations of sphalerite gradually decreases (Figs. 17 and 19B). The δ^{34}S values of red Sp1 fragments range from 1.2 to 3.1 ‰ with an average value of 2.7 ‰ (s.d. = 0.57, n = 8). Seven spot analyses on yellow euhedral Sp2 grains yield δ^{34}S values of 1.2 to 3.0 ‰ with a mean of 2.2 ‰ (s.d. = 0.69). Purple recrystallized Sp3 is deficient in δ^{34}S compared to Sp1 and Sp2, with δ^{34}S values ranging from −3.7 to 1.8 ‰ (mean = -0.1 ‰, s.d. = 1.77, n = 24).

6. Discussion

6.1. Source of ore-forming materials

In principle, two metal and sulfur sources of active seafloor VMS deposit have been proposed as follows: (1) a high-temperature reaction zone (deep > 1 km) within the footwall strata; and (2) a direct magmatic volatile contribution (e.g., Franklin et al., 2005; Martin et al., 2021). Copper, zinc, and gold are primarily transported by sulfur and chlorine ligands in reduced acidic solutions, and sulfur isotope compositions of sulfide minerals can thus offer information on the source, transit, and precipitation of metals, as well as the genesis of VMS deposits (e.g., Franklin et al., 2005; Iizasa et al., 2019). The δ^{34}S values of pyrite and sphalerite from the Huangtupo deposit show a narrow spread, from −3.7 to 5.8‰ (mean = 1.5 ‰, s.d. = 1.81, n = 102), and covers the range of basaltic sulfur (0.1 ± 0.5‰; Sakai et al., 1984). A plausible explanation for the isotopically similar δ^{34}S values of all generations of sulfides is that they were derived from a similar source. Most of the data support a two-component mixed model, where S is sourced from thermochemical sulfate reduction of seawater and the leaching of reduced sulfur from the host rocks. It is possible that there was a significant contribution of sulfur and metals (Cu, Zn, and Au) from the altered intermediate-basic units of the Daliugou Sequence. Mao et al. (2018) reported that the footwall altered basaltic rocks in the Huangtupo deposit are relatively deficient in copper, zinc, and gold compared with the unaltered rocks, which means that the footwall ore-hosted volcanic rocks contributed some of those metals and sulfur. Besides, the widespread development of igneous rocks in the Kalatag area and the lack of large terrigenous sedimentary units suggest that the negative δ^{34}S values are not due to the biogenic reduction of seawater sulfur, but probably to abiotic processes such as redox reactions between sulfate and cations present in reduced form, (such as iron, and copper) (Franklin et al., 2005). This also matches with the occurrence of large amounts of seawater sulfate in the Huangtupo deposit.

In addition, magmatic volatile degassing may also provide an important sulfur source. Since magmatic H_2S and sulfide in volcanic rocks have overlapping values (0 ± 5‰; Franklin et al., 2005), it is not
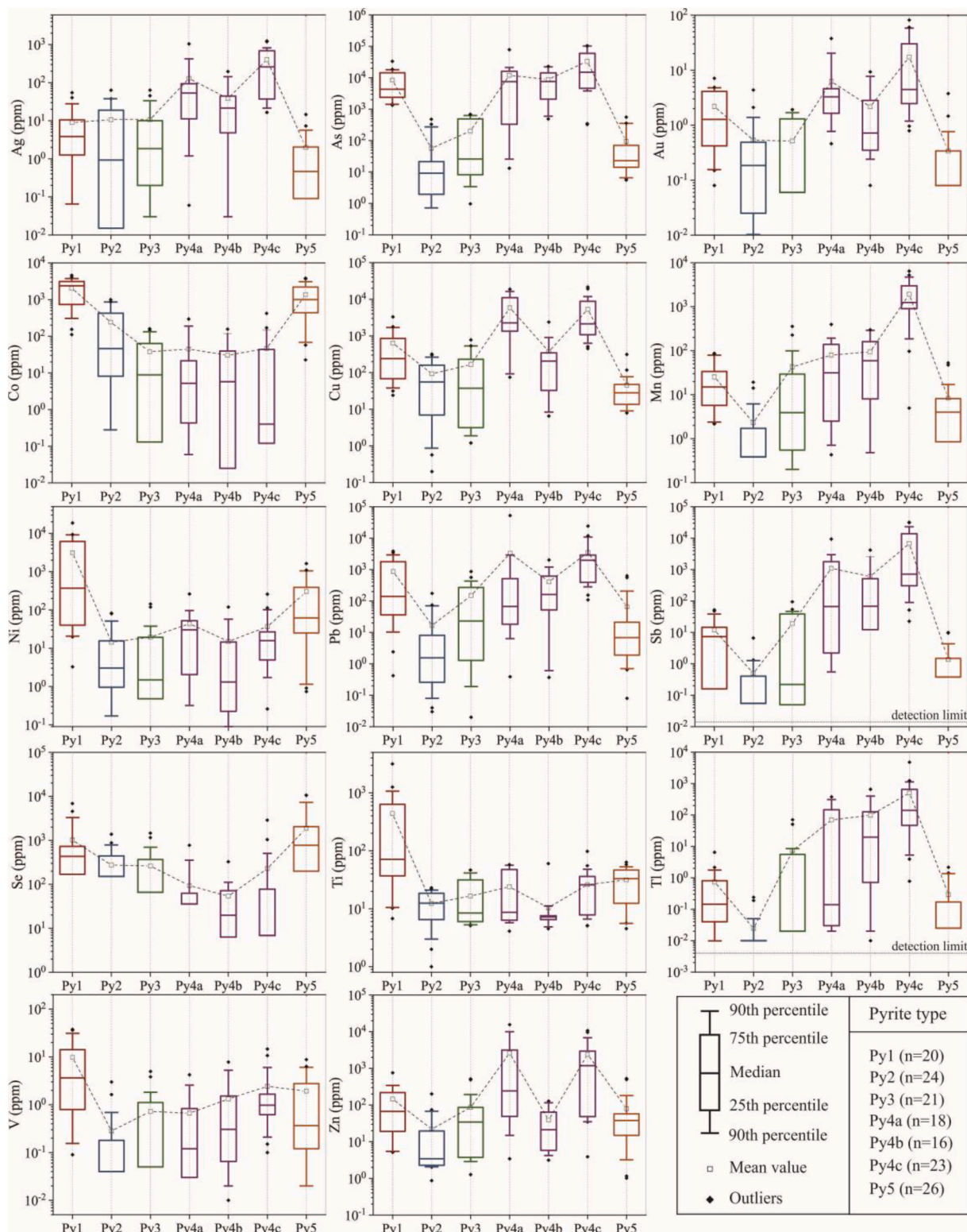
Fig. 10. Statistical representation of the different generations of pyrite analyzed by LA-ICP-MS.

possible to directly distinguish between these two sources. The narrow $\delta^{34}S$ range of Py1 ~ Py3 (-2.3 to 3.1‰) is comparable to diagenetic and hydrothermal pyrite in the underlying Paleozoic magmatic sequences of the Kalatag district (-1.6 to 6.0‰; Deng et al., 2020) and is in the range of magmatic sulfur (0 ± 5‰). The discovery of primary chalcopyrite and pyrite in fresh quartz diorite and H_2S (and possible SO_2) in fluid inclusions also suggests a possible source of magmatic volatile degassing

(Mao et al., 2018; Sun et al., 2020; 2021). Degassing occurred after magma intrusion, sulfur and fluids could have been effectively generated by reactions such as disproportionation of intermediate sulfur species (e.g., S^0, $S_2O_3^{2-}$, or SO_3^{2-}; Habicht et al., 1998; Cheshire and Bish, 2012) or breakdown and desulfidation of pyrite in the underlying Daliugou Formation (Mao et al., 2018).

Overall, the narrow range of sulfide $\delta^{34}S$ values (−3.7 to 5.8‰) is
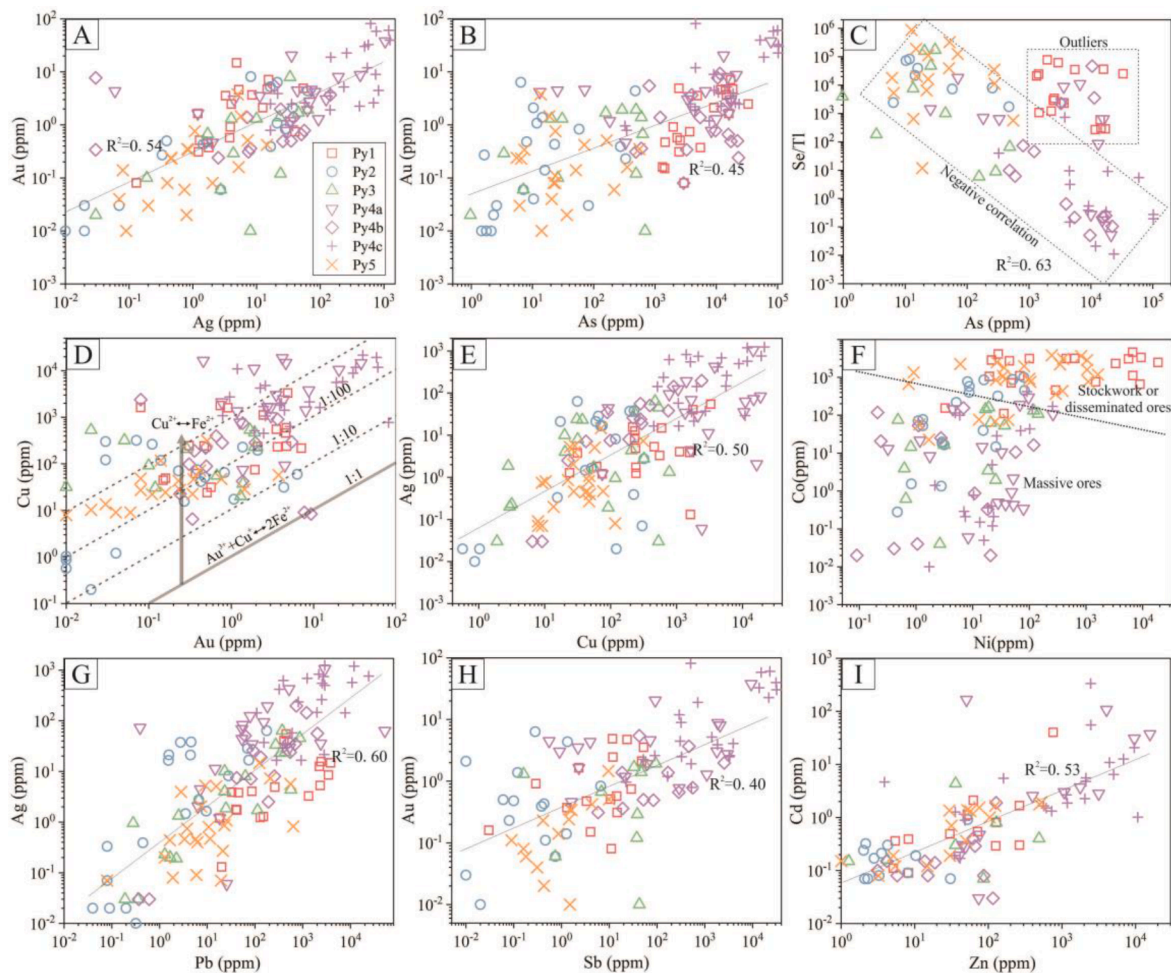
Fig. 11. Plots comparing the concentrations of selected trace elements from different stages of pyrite. Binary plots of Ag and Au (A), As and Au (B), As and Se/Tl (C), Au and Cu (D), Cu and Ag (E), Ni and Co (F), Pb and Ag (G), Sb and Au (H), Zn and Cd (I) in pyrite.
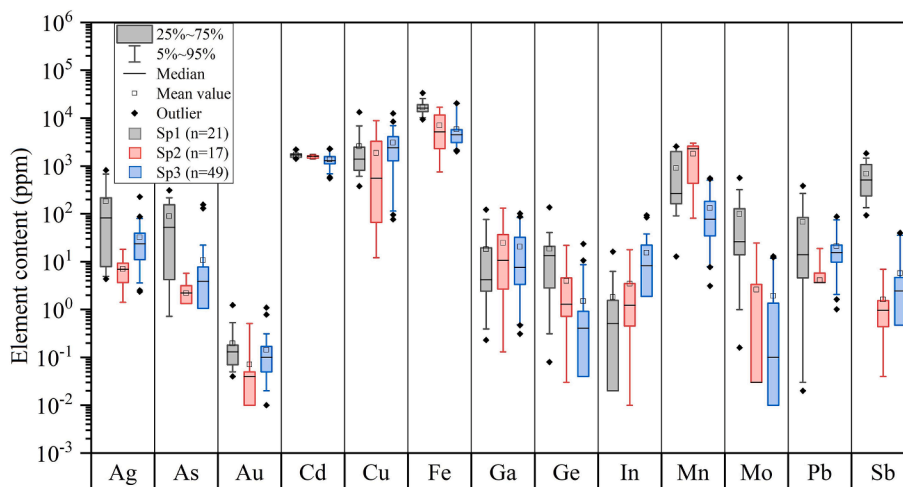
Fig. 12. Concentration boxplot for selected trace elements in Sp1 to Sp3.

comparable to data from other adjacent VMS Cu-Zn-Au deposits (e.g., Huangtan; Sun et al., 2021) and also from elsewhere in the world (e.g., Noranda; Kerr and Gibson, 1993). We conclude from sulfide $\delta^{34}S$ distributions that sulfur in the Huangtupo deposit was mainly derived from inorganically reduced seawater sulfate and host volcanics, with a minor component from a magmatic sulfur source.

6.2. Insights into the mineralization process

Temperature, mineral absorption properties, texture, particle size, fluid composition, fluid mixing, and availability of metal elements and/or S are all possible factors affecting the variation of elements in sulfides (Sykora et al., 2018). Structural and compositional changes in sulfides
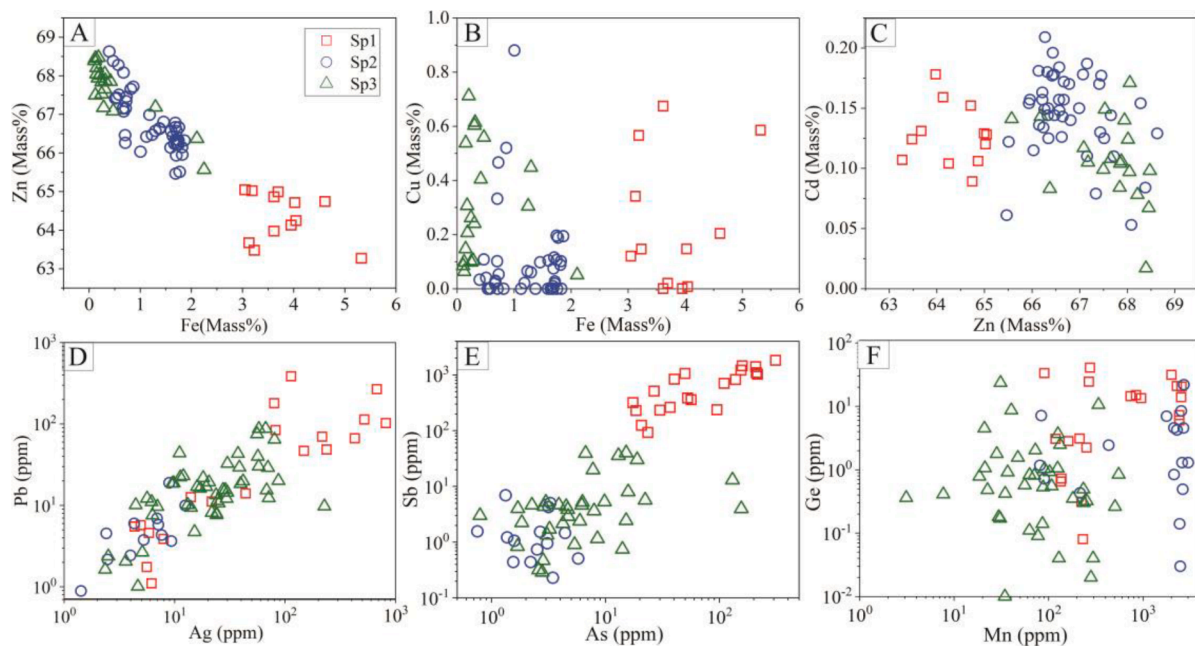
Fig. 13. Binary plots of Fe and Zn (A), Fe and Cu (B), Zn and Cd (C); Ag and Pb (D), As and Sb (E), Mn and Ga (F) in sphalerite derived from the total dataset.
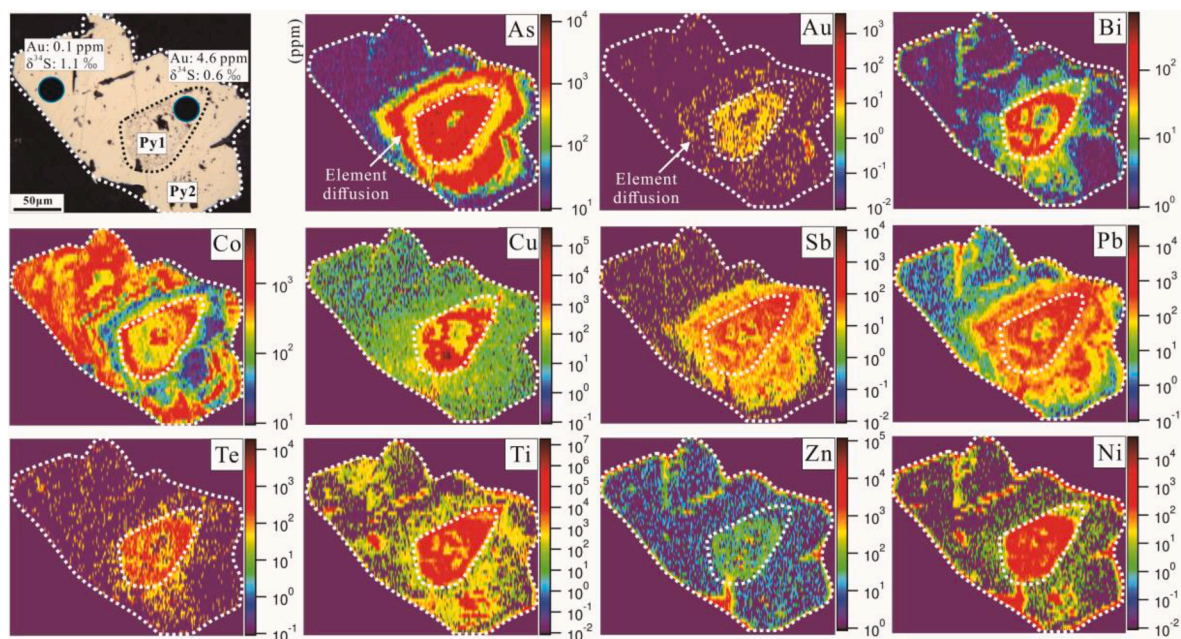
Fig. 14. LA-ICP-MS elemental and interpretative maps of representative pyrite (Py1 ~ 2) grain from SII veined ore (sample YK91-16). The black circle spot represents the laser ablation position.

can also in turn reveal the underlying mechanisms of trace element substitution during mineralization, and the evolution of physicochemical parameters such as temperature and fo_2 (Genna and Gaboury, 2015; Román et al., 2019; Li et al., 2021). A systematic comparison of pyrite and sphalerite microstructures, trace element chemistry and sulfur isotopic signatures suggest that variations in fluid physicochemical condition (e.g., temperature, pH, and fo_2), water–rock reactions, and fluid mixing may play an important role in the Huangtupo VMS mineralization.

6.2.1. Elements controlled by inclusions

Studies have shown that trace elements in mineral particles can occur as lattice substitution, nanoscale inclusions or visible inclusions

(Huston et al., 1995; Deditius et al., 2011). An example is the incorporation of locally supersaturated metals that may be triggered by redox on the surface of pyrite, resulting in the formation of nano- to microscopic inclusions of sulfides and native metals (e.g., Huston et al., 1995; Deditius et al., 2011). Actually, the enrichment of many trace elements can be explained to some extent by the homogenization of inclusions of various minerals previously present in the sulfides, such as chalcopyrite (As, Se), galena (Pb, Bi, Tl), native gold (source of Au and Ag), Bi telluride (Bi, Te), and sulfosalts (As, Sb) (Deditius et al., 2011; Genna and Gaboury, 2015; Melekestseva et al., 2017).

In Huangtupo, the effect of the inclusions on the total trace element content of pyrite and sphalerite is remarkable and the inclusions are not effectively avoided during LA-ICP-MS testing. Sphalerite, chalcopyrite,
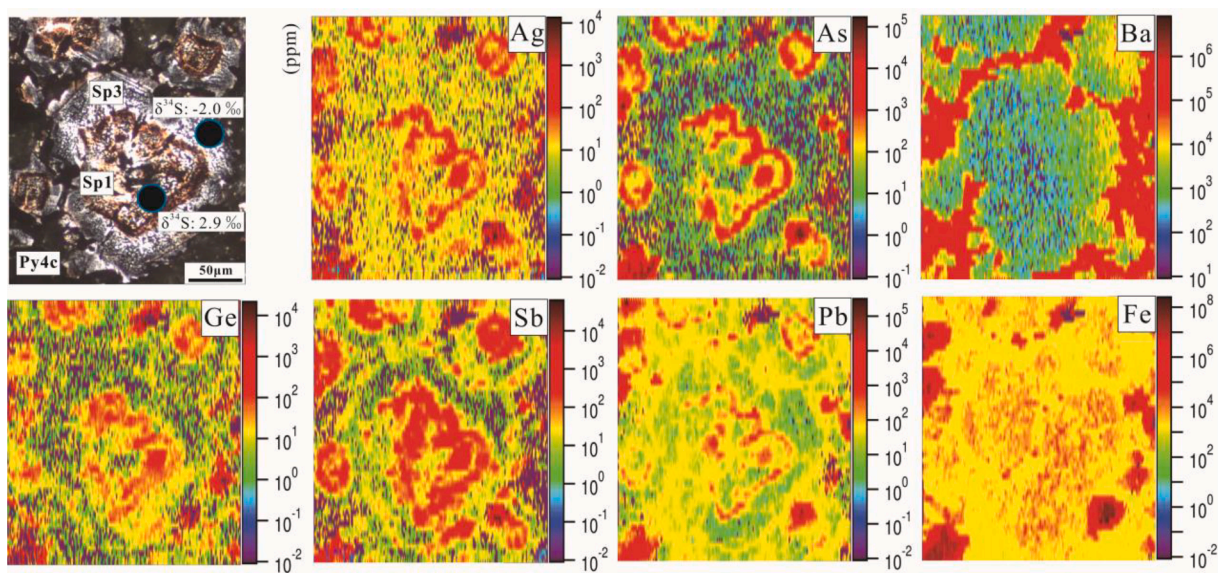
Fig. 15. LA-ICP-MS elemental and interpretative maps of representative sphalerite grain (red Sp1 in the core and mauve Sp3 in the rim) from SIII-2 deformed ore (sample YK111-13). The black circle spot represents the laser ablation position.

Table 4
Laser ablation-multicollector-inductively coupled plasma-mass spectrometry (LA-MC-ICP-MS) in situ sulfur isotopic composition of pyrite and sphalerite from the Huangtupo deposit.

No.	Sample	$\delta^{34}S_{V\text{-}CDT}$(‰)	2σ	Mineral	No.	Sample	$\delta^{34}S_{V\text{-}CDT}$(‰)	2σ	Mineral	No.	Sample	$\delta^{34}S_{V\text{-}CDT}$(‰)	2σ	Mineral
1	YK94-17	−0.2	0.1	Py1	35	YK94-14	2.2	0.3		69	YK91-12	1.2	0.2	
2	YK94-17	−0.4	0.1		36	YK94-14	1.5	0.2		70	YK111-13	3.1	0.2	
3	YK94-17	−2.3	0.3		37	YK94-14	2.0	0.1		71	YK111-13	2.9	0.2	
4	YK94-17	−1.9	0.2		38	YK91-9	3.2	0.3	Py4a	72	YK91-10	2.4	0.1	Sp2
5	YK91-16	0.6	0.1		39	YK91-9	2.5	0.2		73	YK91-10	2.8	0.3	
6	YK91-16	0.9	0.2		40	YK91-10	5.0	0.3		74	YK91-10	3.0	0.3	
7	YK91-17	1.1	0.2		41	YK91-10	5.2	0.3		75	YK91-10	1.7	0.2	
8	YK91-17	0.9	0.2		42	YK91-10	5.0	0.3		76	YK111-18	1.2	0.3	
9	YK111-29	1.5	0.3		43	YK111-13	1.7	0.2	Py4b	77	YK111-18	3.0	0.2	
10	YK111-29	1.7	0.1		44	YK111-13	2.5	0.2		78	YK111-18	1.5	0.3	
11	YK111-29	2.3	0.1		45	YK111-13	3.3	0.3		79	YK91-10	1.8	0.3	Sp3
12	YK111-29	1.8	0.2		46	YK91-10	4.2	0.4		80	YK91-10	1.7	0.2	
13	YK111-20	2.6	0.3	Py2	47	YK91-10	4.7	0.2		81	YK91-10	1.5	0.2	
14	YK111-20	2.2	0.2		48	YK91-10	4.9	0.2		82	YK91-10	0.9	0.2	
15	YK111-20	3.1	0.3		49	YK91-10	5.8	0.1	Py4c	83	YK91-10	0.5	0.1	
16	YK94-14	0.9	0.3		50	YK91-10	4.5	0.3		84	YK91-10	0.4	0.2	
17	YK94-14	0.6	0.2		51	YK91-10	3.6	0.3		85	YK91-10	0.6	0.2	
18	YK94-14	0.6	0.3		52	YK111-12	3.9	0.2		86	YK91-9	−0.4	0.4	
19	YK94-10	0.7	0.2		53	YK111-12	3.5	0.3		87	YK91-9	1.0	0.2	
20	YK94-10	0.8	0.3		54	YK111-12	2.8	0.2		88	YK91-9	0.4	0.2	
21	YK94-10	0.7	0.1		55	YK91-6	2.4	0.3	Py5	89	YK91-9	0.2	0.3	
22	YK91-14	1.2	0.3		56	YK91-6	2.8	0.3		90	YK91-9	1.0	0.2	
23	YK91-14	0.5	0.3		57	YK94-1	2.6	0.1		91	YK91-9	1.9	0.2	
24	YK91-14	1.1	0.4		58	YK94-1	0.9	0.3		92	YK91-9	1.1	0.2	
25	YK91-14	0.0	0.2		59	YK94-1	1.5	0.3		93	YK111-12	−0.1	0.3	
26	YK91-14	0.7	0.2		60	YK111-3	0.4	0.3		94	YK111-12	0.0	0.3	
27	YK91-14	0.0	0.3		61	YK111-3	1.5	0.2		95	YK1 11–12	−2.9	0.2	
28	YK111-17	2.3	0.2	Py3	62	YK111-3	0.9	0.3		96	YK111-12	−3.1	0.2	
29	YK111-18	−0.3	0.2		63	YK111-3	1.8	0.3		97	YK111-12	−2.3	0.3	
30	YK111-18	1.1	0.3		64	YK91-14	3.0	0.2	Sp1	98	YK111-12	−3.5	0.1	
31	YK112-15	1.8	0.1		65	YK91-14	2.7	0.3		99	YK111-13	−2.0	0.3	
32	YK112-15	2.0	0.2		66	YK91-14	3.0	0.2		100	YK111-13	1.8	0.4	
33	YK112-15	1.5	0.3		67	YK91-12	2.8	0.2		101	YK111-13	1.1	0.2	
34	YK112-15	1.8	0.3		68	YK91-12	3.0	0.2		102	YK111-13	−3.7	0.3	

V-CDT = Vienna-Canyon Diablo Troilite.

and galena are the main visible sulfide inclusions in most generations of pyrite (Fig. 16B). The siderophile and chalcophile elements, such as As, Co, Ni, Cu, Pb, and Se, show obvious variation in concentration (Fig. 10). Usually, sphalerite can incorporate considerable concentrations of Cd, Ge, and Ga, while galena can contain significant amounts of Ag, Sb, and Bi (Bowles et al., 2011). The positive correlation between Zn and Cd (R^2 = 0.53) indicates that Cd in pyrite is typically from sphalerite inclusions (Fig. 11I). Chalcopyrite can be enriched in Ag (substituting for Cu), Sn, and Zn (Huston et al., 1995). Statistically, Cu has varying degrees of correlation with Ag ($R^2 = 0.50$), Au ($R^2 = 0.45$), and As ($R^2 = 0.54$), suggesting that chalcopyrite inclusions influence these elements in pyrite (Fig. 11D, E). A possible explanation is coupled substitutions, such
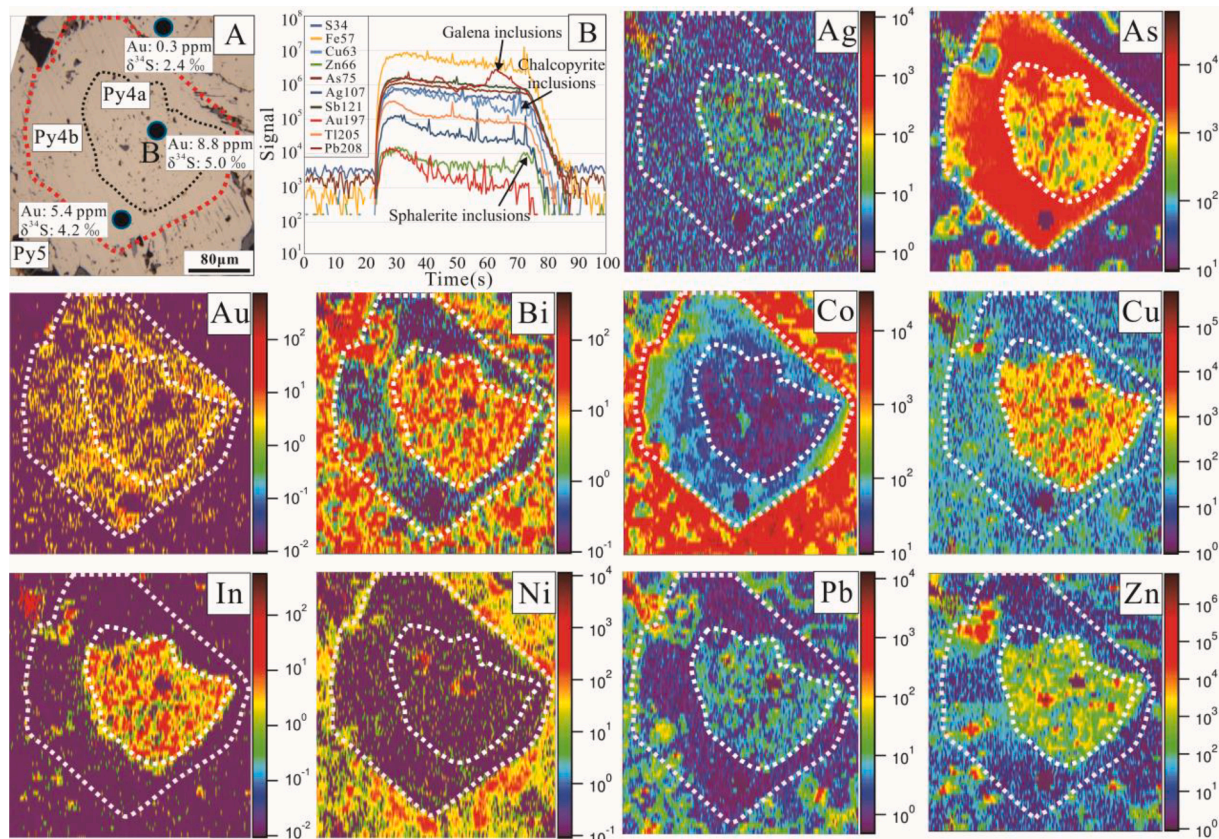
Fig. 16. LA-ICP-MS elemental and interpretative maps of representative pyrite (Py4 ~ 5) from SIV recrystallized disseminated magnetite - pyrite ore (A; sample YK91-6); B. Typical inductively coupled plasma-mass spectrometry count output for Py4a analyses by laser ablation. The black circle spot represents the laser ablation position.
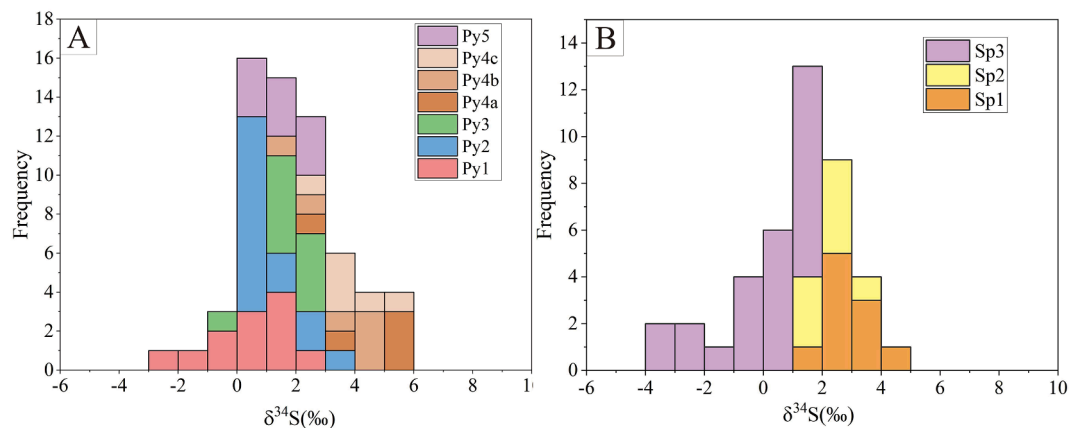

Fig. 17. Histograms showing range of sulfur isotope values of various generations of pyrite (A) and sphalerite (B) at Huangtupo.

as Au-Cu for Fe^{2+} (Fig. 11D; Chouinard et al., 2005). Besides, the Fe content of sphalerite obtained by EPMA analysis gradually decreased from early to late stages (Electronic Appendix Table A3), while Cu content changed on the contrary, which is confirmed by the LA-ICP-MS analysis. This also indirectly illustrates the influence of chalcopyrite inclusions within sphalerite on elemental distribution (Figs. 12 and 13A-B). Positive Ag, Bi, Sb, and Pb correlations also indicate that Ag, Bi, and Sb are present in galena inclusions (Fig. 13D-E). The positive correlation between Au and Ag, Cu, Pb, Sb indicates that gold in pyrite mostly exists in the form of mineral inclusions (Fig. 11A, D, H). However, galena is not abundant in this deposit and only controls a limited amount of trace elements.

In addition, a significant number of silicate inclusions from the host lithology have been observed in many pyrite grains. Ti (titanite), V (magnetite), Mn, and Ba (feldspar and other silicates) are elements that are likely related to silicate and oxide inclusions (e.g., Fig. 6G, H; Mathieu, 2019).

6.2.2. Physicochemical environment reconstruction of the trace element in pyrite and sphalerite

Pyrite: During the preore stage, internal overpressuring and fracturing may occur as a result of magmatic volatile exsolution accompanying the rapid crystallization of subvolcanic intrusions. Magmatic-hydrothermal fluids and volatile elements, such as Au, As, Sb, Te, Ag,
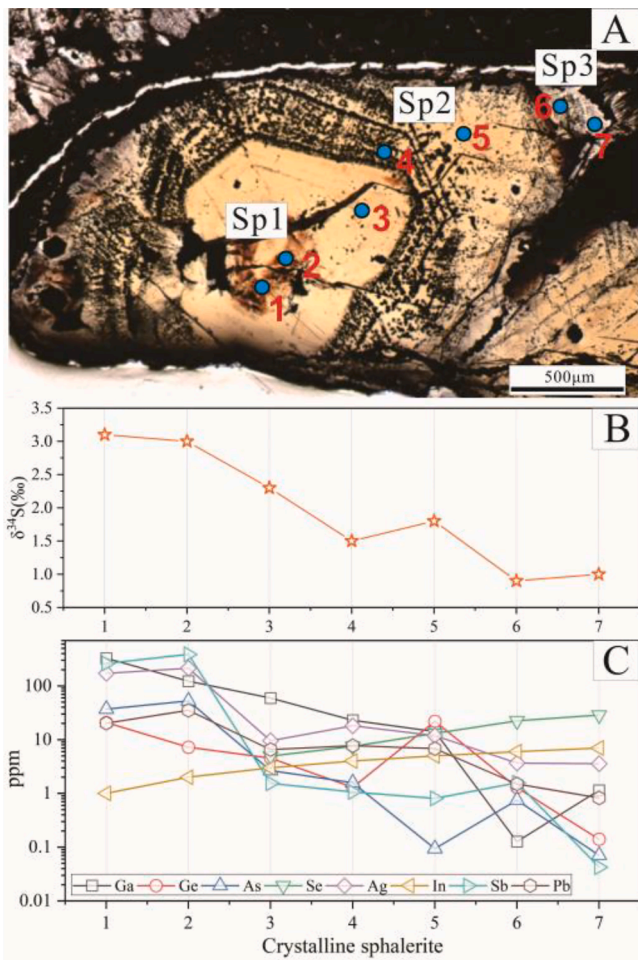
Fig. 18. A. Transition from residual Sp1 at the core to crystalline Sp2 ~ 3 at the edge; B. In-situ sulfur isotope variation (LA-MC-ICP-MS) from Sp1 to Sp3; C. Trace element variations (LA-ICP-MS) from Sp1 to Sp3. Blue circle spots represent in situ sulfur isotope positions.

S, and Se, can be transported outside the intrusion environment via outward propagating fractures, in which they may merge with a seawater convection system. Metals and sulfur are initially enriched in the bottom basaltic volcanic rocks through high-temperature interactions between modified seawater and rocks (Fig. 20A; Franklin et al., 2005). Cobalt, Ni, Bi, Se, Cu, and Te, in general, are temperature-sensitive elements and are usually enriched in high-temperature precipitated sulfides (~400℃; Figs. 10 and 14; Wohlgemuth-

Ueberwasser et al., 2015; Keith et al., 2016b). In comparison to other sulfide generations (Py2 to Py4), the porous nature of Py1 and the abundance of these elements (Fig. 10) indicate rapid nucleation in a high-temperature acid fluid mediated environment (pH: 3 ~ 4; e.g., Franklin et al., 2005; Putnis, 2009). The element suite in Py1 is similar to that of pyrite at Skouriotissa hydrothermal upflow zone (~400℃), Cyprus, as reported by Keith et al. (2016a). In this environment, many soluble trace elements are not incorporated into the pyrite structure, except Co and Ni, which have been shown to replace Fe stoichiometrically in pyrite at 400℃, and potentially Se and Te, which replace S (Fig. 10; e.g., Huston et al., 1995). Or, elements with an affinity for low-temperature fluids, such as Sb, are partitioned and refined out, leaving only the metals that are stable at 400℃.

During the SII, upward migrating magmatic-hydrothermal fluids mixed with limited convective seawater in *syn*-volcanic faults (e.g., F2) within the Daliugou Formation (Fig. 20B). This process caused a strong fluid-rock interaction, accompanied by a significant drop in fluid temperature (~300℃; Determined by the geothermometer: $\triangle^{34}S_{Py-Ccp} = 4.5 \times 10^6/T(K)^2$; Kajiwara and Krouse, 1971) and a rise in pH, which eventually led to the precipitation of stockwork pyrite-chalcopyrite ores. The subhedral shape and corroded boundary of Py1 surrounded by Py2 in the stockwork zone suggest the dissolution of Py1 during or prior to Py2 crystallization (Fig. 3). The LA-ICP-MS elemental maps reveal distinctly low and heterogeneous trace element contents in Py2, except for Co (Figs. 10 and 14). This may be due to a deficit of trace elements in early hydrothermal fluids, or the preferential incorporation of trace elements in fluids into other minerals (e.g., chalcopyrite), or the formation of accessory mineral phases (e.g., Ag-Au bearing minerals; Genna and Gaboury, 2015). Of these, the first two speculations are the most plausible, as the sulfides coeval with Py2 in the vein ore are generally deficient in trace elements, while the chalcopyrite in them is relatively more enriched in trace elements (Pan, 2019).

During the main ore period, seawater mixed extensively as the magmatic-hydrothermal fluids continued to ascend and mature, which also led to the deposition of large amounts of sulfide near the seafloor. Analysis results show that the $\delta^{34}S$ value of pyrite increases from 0.5‰ to 4.2‰ from SI to SIII-2, which may be attributed to the incorporation of seawater-derived S in the mixing of the fluid with seawater (Fig. 19A; Janecky and Shanks, 1988). Quartz H-O isotope studies also support a dominantly magmatic fluid signature and were diluted by deeply circulating seawater (Deng et al., 2020). The main ore stage of the Huangtupo deposit consists of two main fluid phases (Fig. 5). Fluid-phase I formed in SIII-1 is dominant in the history of seafloor convective systems. It underwent long-term cyclic extraction of the surrounding rocks and was responsible for medium to high-grade chalcopyrite and pyrite massive ores, as well as Zn-Cu veinlets with no apparent Au phases. The similarity of trace element signatures and mineral assemblage of Py3 and Py2 shows that they are genetically related, with
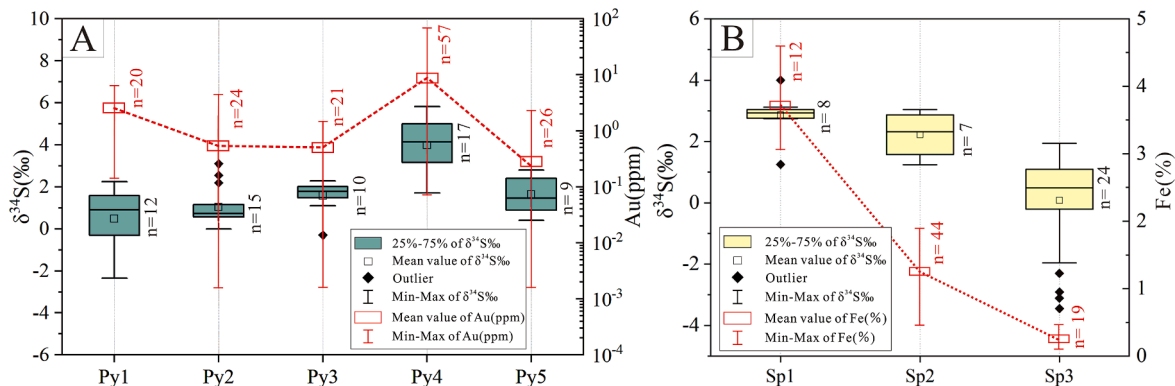

Fig. 19. Variations in sulfur isotope range and mean Au content of pyrite (A) and mean Fe content of sphalerite (B) from the Huangtupo deposit. The red dashed line represents the broken line of the mean value of gold content in pyrite at each stage.
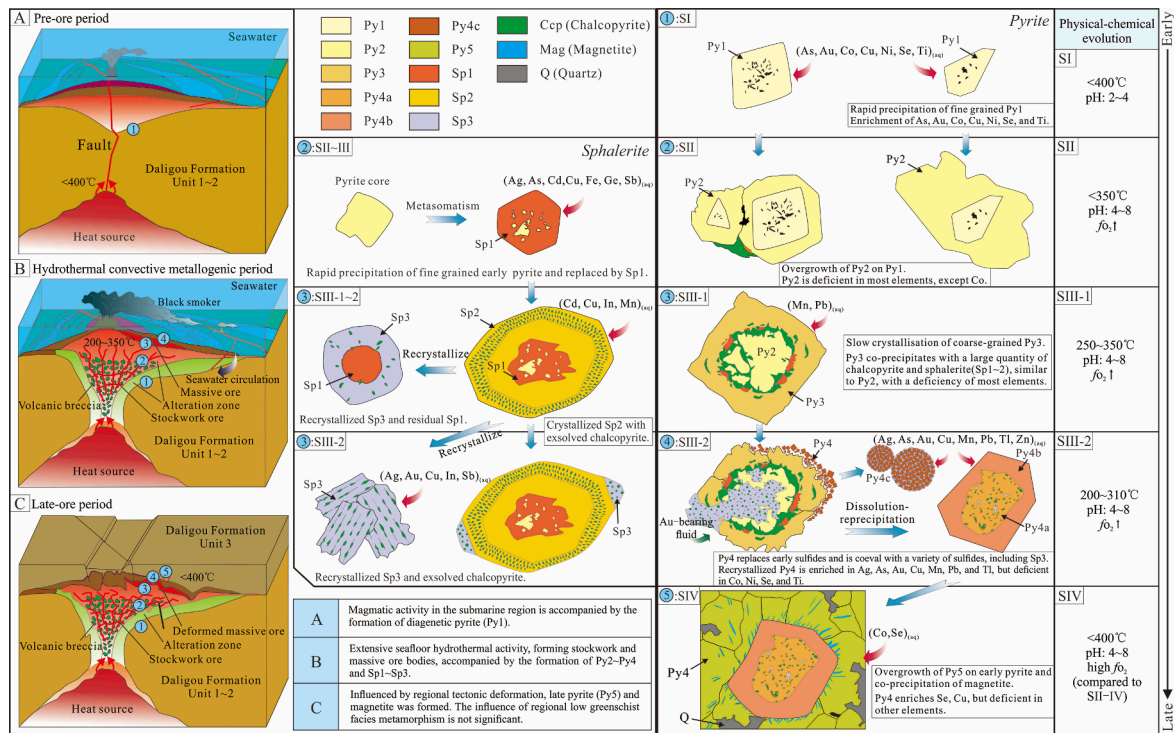
Fig. 20. Schematic cartoon of the mineralization model (left, including A ~ C) and trace element compositions of pyrite and sphalerite during the evolution of the Huangtupo hydrothermal system (right). Cartoon diagrams of sphalerite and pyrite grains representing different evolutionary stages were selected to illustrate the evolution of mineral textures, trace elements and mineral assemblages. The pH values are referenced from Genna and Gaboury, 2015 and Franklin et al., 2005.

similar fluid compositions and precipitation conditions. A possible explanation for the scarcity of trace elements in Py3 is its formation in a stable hydrothermal environment. This is because rapid crystallization facilitates trace element mixing and adsorption to the pyrite surface, while at slower crystallization rates, Fe and S atoms more readily displace other ions to form a thermodynamically more stable, but trace element-deprived, pure pyrite (Abraitis et al., 2004; Sykora et al., 2018). The low Co, Ni, and Se contents in massive ores-hosted pyrite (Py3) possibly indicate fluid temperatures below 300℃ (250 ~ 300℃; Geothermometer:$\triangle^{34}S_{Py-Sp} = 3.0 \times 10^6/T(K)^2$; Kajiwara and Krouse, 1971) compared to higher precipitation temperatures in the stockwork ore zone (Keith et al., 2016a) where these metals are concentrated.

The Au and Ag contents in Py4a ~ c increased significantly in the SIII-2, which may be a new hydrothermal (fluid-phase II, 240 ~ 310℃; Geothermometer:$\triangle^{34}S_{Py-Gn} = 1.1 \times 10^6/T(K)^2$; Electronic Appendix Table A6; Kajiwara and Krouse, 1971) superimposed injection during regional tectonic activity (Deng et al., 2016, 2020). The strong metasomatism of early sulfides by this phase of fluids, accompanied by orebody deformation and local metamorphism (Fig. 6E, k), may have led to the mobilization and migration of trace elements (e.g., Zn, Cu, Pb, Au, and Ag) from the early ore. The fluctuation of fo_2 and temperature decrease during fluid phase II caused the dominant sphalerite, chalcopyrite, and arsenic pyrite mineral deposition with minor pyrrhotite, and trace tetrahedrite - galena - gold mineral observed in quartz veins (Fig. 8; Li et al., 2021). The patchy As zonation and abundant sulfide inclusions in the porous Py4a indicate crystallization in a fluid-dominated rapid precipitation environment (Fig. 16; Román et al., 2019). It mainly contains galena, sphalerite, and chalcopyrite inclusions (Fig. 16B), which are most likely dissolved from previous sulfides and reprecipitated as individual grains (appearing as tiny inclusions) driven by saturation during dissolution-reprecipitation (e.g., Saravanan et al., 2020). A similar phenomenon is common in pyrite and sphalerite within VMS deposits worldwide (e.g., Ye et al., 2011; Genna and Gaboury, 2015; Wohlgemuth-Ueberwasser et al., 2015; Liu and Beaudoin, 2021). In contrast, the Py2-3 mostly maintains its original euhedral crystal form

with almost no microinclusions and pores, and low As, Au, Ag, Co, and Ni content, indicating that they were formed under relatively gentle and stable fluid conditions (Fig. 11A-H; Román et al., 2019).

At Kalatag, magnetite and hematite are predominantly disseminated and veined within the massive ore body and overlying volcanic rocks, probably related to the late high temperature (up to 400 °C; Geothermometer:$\triangle^{34}S_{Py-Ccp} = 4.5 \times 10^6/T(K)^2$), relatively high oxygen fugacity hydrothermal fluids (Galley et al., 2000; Sharpe and Gemmell, 2002; Genna and Gaboury, 2015). High-temperature fluid replaced only small amounts of early sulfides, especially massive pyrite, leading to the exclusion of trace elements. The resulting recrystallized pyrite is deficient in most trace elements, but relatively enriched in high-temperature elements such as Co, Ni, and Se (Fig. 10; Huston et al., 1995). Similarly, Genna and Gaboury, (2015) and Boucher, (2011) observed comparable results at the Bracemac-McLeod and Ansil West deposit, where the pyrite and magnetite that replaced earlier sulfides were deficient in most trace elements. Overall, the evolution of hydrothermal fluids to more oxidized conditions may be due to the injection of more oxidized magma and may be triggered by the regional or localized conversion of tectonic systems.

Sphalerite: Sphalerite is one of the most important metallic minerals in the main ore stage (SIII). Its structural and compositional variations in combination with pyrite can reflect additional mineralization information. In Huangtupo, sphalerite from different generations varies significantly in color and trace element content. For example, the darker red Sp1 from Huangtupo contains higher Ag, As, Cd, Ge, and Sb than lighter Sp2 ~ 3, which can also be observed in the elemental maps (Fig. 15). Studies have also shown that the presence of metals such as Ag and Cu may improve the capacity to incorporate other trace elements (Cook et al., 2009; Belissont et al., 2014), which explains the relative enrichment of elements such as As, Sb, Ge and Au in Sp1 (Fig. 12). The enrichment of these elements in Sp1 is likely to be related to the chalcopyrite micro-inclusions (Pfaff et al., 2011). Moreover, grain size, and the presence of organic matter may also affect the color of sphalerite (e. g., Pfaff et al., 2011), which may also indirectly reflect the physical and chemical environment of the mineralization process.

Fe is the most abundant trace element in sphalerite. The variation of Fe content in sphalerite is mainly related to the Fe-Zn replacement caused by the fluctuation of hydrothermal fs_2 and fo_2 and the increase and decrease of temperature (Hutchison and Scott, 1983; Keith et al., 2014). The gradual decrease in Fe content (EPMA data; Figs. 12 and 13A) from Sp1 to Sp3 indicates that the sulfur and/or oxygen fugacity increased, or temperature decreased, or both, from the early to late main ore stage in the Huangtupo deposit (e.g., Scott and Barnes, 1971). However, the calculated temperatures show a tendency to decrease and then increase from Sp1 to Sp3, with a range of ca. 260 to 300 °C for Sp1, ca. 220 to 250 °C for Sp2, and ca. 230 to 260 °C for Sp3 (Fe/Zn$_{sphalerite}$ = 0.0013(T)−0.2953; Keith et al., 2014). We excluded the sphalerite geothermometer proposed by Frenzel et al. (2016) due to the abundance of inclusions in the sphalerite, resulting in large differences in the Ga, Ge, Mn, and In content data obtained by LA-ICP-MS. These calculated temperatures match the fluid inclusion data, which yields peak homogenization temperatures ranging from 200 to 320 °C (Cheng et al., 2020). The pyrite coeval with sphalerite at each stage also shows a matching property.

6.3. Gold deportment

Although gold is not the major metallogenic element in the Huangtupo deposit, the gold enrichment process may provide some clues to the genesis of other gold-rich VMS deposits. Ore mineralogy and element mapping consistently provide evidence for multi-stage mineralization events at the Huangtupo deposit, in which two distinct types of gold introduction are proposed. The Au content (2.68 ppm on average) in the sparsely disseminated Py1 in the surrounding rocks is significantly higher than the massive ore body, which represents the earliest enrichment of gold. Studies have shown that the plot of Se/Tl versus As can be used to distinguish between pyrites of hydrothermal genesis and pyrites formed during regional metamorphism (Genna and Gaboury, 2015). Se/Tl versus As has a good correlation in hydrothermal pyrite, while Se/Tl versus As data in metamorphic pyrite deviate from the group (Fig. 11C). This suggests that regional metamorphism in the low greenschist facies may be the dominant factor in the initial Au enrichment.

Later gold mineralization is primarily related to Py4 and Sp3 with the highest gold abundance. Unlike Py1 (SI), Py4 and Sp3 (SIII) contain many visible gold inclusions. Porous Py4 and Sp3 coexist with electrum in veinlet ores and contain a mean of 9.5 and 0.2 ppm Au, respectively, which is markedly higher than that of Py2 ~ 3 and Sp1 ~ 2 in massive ores (Table 2). It is well known that most ancient VMS deposits are overlain by deformation and metamorphism and are the product of widespread post-VMS uplift, basin inversion, and compression (e.g., Castroviejo et al., 2011; Duuring et al., 2016; Yu et al., 2020). These processes have the potential to alter the geometry and distribution of the orebody, resulting in sulfide remobilization, recrystallization, cataclastic deformation, and/or overgrowth of multiple generations of sulfides (e.g., Brueckner et al., 2016; Yu et al., 2020). In the Huangtupo deposit, the massive orebodies were staggered by retrograde and strike-slip faults during regional compression, and the altered rocks carrying the massive orebodies also underwent structural deformation in the process, forming deformation structures such as boudinage, pressure shadows, and folds in the siliciclastic rocks (XXMCL, 2009; Mao et al., 2015; 2018). Affected by regional deformation during SIII-2, new fluids at depth rapidly came upward and extracted numerous trace elements in the early ore and volcanic rock (including Au, Ag, Cu, etc), forming a series of irregular sulfide veinlets (Fig. 8A) in the enclosing rocks and massive ores. As shown in Fig. 11C, the formation of SIII-2 gold-rich pyrite is also affected by local metamorphism (Genna and Gaboury, 2015).

Usually, low to neutral pH, near seawater salinity, and moderately reducing conditions are typical for gold transport in seafloor hydrothermal fluids (Benning and Seward, 1996; Hannington et al., 2016). In

the H2S-dominated hydrothermal environment during the SIII-2, the close mineralogical association of the Ag-rich electrum with sphalerite, chalcopyrite, and pyrite suggests that Au was transported in a reduced fluid by bisulfide complexes (such as $Au(HS)_2^-$ and $HAu(HS)_2^0$) at a temperature <300 °C (e.g., Williams-Jones et al. 2009; Brueckner et al. 2016; Liu and Beaudoin, 2021). By reaction 1, the solubility of gold can be increased with decreasing pH in oxidizing fluids (Gammons and Williams-Jones 1995).

$$Au_{(s)} + 2H_2S_{(aq)} + \tfrac{1}{4}O_{2(g)} = Au(HS)_2^- + H^+ + \tfrac{1}{2}H_2O \qquad (1)$$
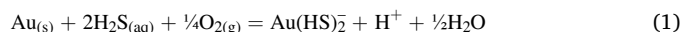
The deposition of gold likely caused by the mixing of reduced hydrothermal fluids with oxygenated sulfate-rich ambient seawater, resulting in the oxidation of $Au(HS)^{-2}$ and a decrease in H_2S content ((Hannington and Scott, 1989; Huston et al., 1992). The abundance of inclusions and framboidal textures in Py4a ~ c and Sp3 associated with gold concentrations are attributed to relatively high nucleation and growth rates at high degrees of FeS_2 supersaturation (e.g., Farrand, 1970; Román et al., 2019). Besides, the replacement of early sulfides and leaching of surrounding rock also occur during this process, which is why pyrite in SIII-2 is partially affected by metamorphism (Fig. 11C). The replacement of earlier sulfides by later fluids can cause elemental remobilization, such as the changes in elemental content of Au, As, and Cu exhibited by the replacement of Py1 by Py2 (Fig. 14). In this process, coupled dissolution-reprecipitation is the most common reaction and mobilization mechanism of elements (e.g., Liu and Beaudoin, 2021). The presence of sharp interfaces between Sp3 and Sp2 (Fig. 7E) and the presence of abundant polymineralic inclusions between Py4a ~ c (Fig. 6L, M) is also indirect evidence that it is generated by repeated coupled dissolution and reprecipitation (Fig. 16; Liu and Beaudoin, 2021).

Although high-grade ores (up to 66 ppm Au) were formed from this gold enrichment event, they were limited in quantity and only enriched in some veined Cu-Zn ores (Fig. 8A) and deformed ores (Fig. 6E, K) at the top of massive ore bodies. This may imply that the overprinting by a short-lived penecontemporaneous hydrothermal event may be linked to gold enrichment in some VMS deposits (Franklin et al., 2005). Such a gold enrichment is described in other gold-rich VMS systems, such as the Ming (Canada) and Boliden (Sweden) VMS deposits (Mercier-Langevin et al., 2013; Brueckner et al., 2016; Liu and Beaudoin, 2021).

6.4. Genetic model for the Huangtupo Cu -Zn-Au deposit

Although the Kalatag area has undergone multiple periods of mineralization, the temporal relationship between the lower stockwork mineralization and the upper massive mineralization of the Huangtupo deposit has already been constrained to the Early Silurian (Deng et al., 2016; 2020). Precise magmatic and mineralization ages, as well as mineralogical and isotopic signatures, support an Early Paleozoic submarine volcanism-related origin for the Cu-Zn-Au deposits surrounding the Kalatag intrusion, as several contemporaneous submarine volcanoes have been identified (Mao et al., 2018). For example, Deng et al., (2016) and Sun et al., (2020) reported a reliable Re-Os isochron age of adjacent Hongshi and Huangtan deposits, which is 429.8 ± 5.9 Ma and 437.9 ± 6.6 Ma, respectively. The mineralization ages of the Huangtupo (Re-Os age: 432.2 ± 3.1 Ma; Yang et al., 2018) and these deposits all match the zircon ages of the Kalatag pluton and marine volcanic rocks (452 ~ 427 Ma; Sun et al., 2019). Geophysical evidence suggests that subvolcanic intrusions exist at depth beneath these deposits (XXMCL, 2009), which are considered to be heat sources for driving convective fluid.

In the SII, deep-seated magmatic ore fluids discharged from regional tensile faults, such as the Kalatag fault and its secondary faults (F1 ~ F3), were channeled beneath the high-permeability seals formed by Daliugou intermediate-acid volcaniclastic rock that cap the hydrothermal system, resulting in a dispersed reaction of fluids with preexisting sulfides (Py1) in Unit 1 of Daliugou Formation. The extensive volcanic

brecciation between the Ordovician-Silurian volcanic series offered a channel for metal deposition of ore-bearing fluids. The resulting ascending hot, acidic, reduced fluids transported S and predominantly metallic elements that precipitated within the breccia cracks as coarse pyrite (Py2) because of either physical or chemical processes. During the SIII-1, the continuous upwelling of metal-bearing fluids mixed with the infiltrated seawater leads to a rapid drop in temperature and pressure, which continues to produce fluid phase separation and rapid precipitation of sulfides (Py2 ~ 3 and Sp1 ~ 2) in the metal-rich fluids. This stage of mineralization is mainly in the form of cement filling between fissures or precipitated accumulation of massive sulfides on the seafloor. Accompanied by orebody deformation and local metamorphism, the main gold metallogenic process (associated with Py4 and Sp3) within the deposit is associated with a new short-lived hydrothermal event (SIII-2), which leached and re-enriched gold from earlier sulfide and gold pre-enriched surrounding rocks. In many cases, gold can be mobilized to the peripheral or internal sulfide veinlets of the VMS deposit during deformation and metamorphism (e.g., Eastern Australian VMS deposits: Huston et al. 1995; Boliden, Sweden: Mercier-Langevin et al., 2013) or late hydrothermal remobilization (e.g., Ansil deposit, Quebec: Galley et al. 2000). These processes typically result in significant gold enrichment and upgrading of the deposit. However, multiple or persistent similar fluid events are required to form a larger scale and volume of gold mineralization. Systematic in situ studies of pyrite and sphalerite within the deposit can precisely reveal the metal origin and fluid evolution of an ancient VMS deposit, which is difficult to achieve with conventional bulk-rock analysis. The detailed ore-forming process of the Huangtupo deposit is summarized in Fig. 20. In addition to this, The Huangtupo deposit formed in an Early Paleozoic immature intra-oceanic arc (Mao et al., 2018), and VMS deposits in this setting are usually characterized by clustered and zoned distribution. Similar VMS deposits of copper, zinc, and gold, such as the Huantan-Jinling VMS deposit, have been discovered near the Huangtupo in recent years (Fig. 2; Sun et al., 2020). As a unique bedrock outcrop regionally, the establishment of its metallogenic model in the Kalatag area can effectively guide the discovery and exploration of similar deposits in the peripheral Gobi-covered area.

7. Conclusions

The Huangtupo Cu-Zn (Au) deposit is hosted in the Ordovician-Silurian intermediate to acid volcanic, volcaniclastic rocks in the ETOB. Results of in-situ sulfur isotope and LA-ICP-MS trace element analysis indicate that the sulfur and metal in the hydrothermal system were most likely originally sourced from inorganically reduced seawater sulfate and host volcanics with minor contributions of magmatic volatiles.

The Huangtupo deposit recorded multi-stage hydrothermal mineralization. Five pyrite and three sphalerite types were identified. The chemical composition (especially As, Co, Ni, Pb, Se of pyrite and Fe, Cu, Mn, and Sb of sphalerite) and textures of these sulfides are indicative of the vertical fluctuating changes in temperature, pH, and fo_2 during their precipitation at the scale of an ancient VMS deposit. The multi-stage upwelling of fluid is related to the emplacement of the Early Paleozoic Kalatag subvolcanic intrusions. Continued and repeated sulfide precipitation in the hydrothermal circulation system is important for the formation of massive Cu-Zn ore bodies. Detailed LA-ICP-MS elemental mapping and sulfur isotope analysis provide persuasive evidence for the introduction of a short-term, gold-rich fluid that re-enriched gold by dissolving and reprecipitating trace elements from earlier ores and surrounding rocks. Regional deformation- triggered hydrothermal activity and local metamorphism played a key role in this gold enrichment event. This situation may apply to many gold-rich VMS-type deposits. A metallogenic model is established for ore prospecting in the peripheral Gobi-covered area.

Appendix A. Supplementary data

Supplementary data to this article can be found online at https://doi.org/10.1016/j.oregeorev.2023.105475.

References

Abraitis, P.K., Pattrick, R.A.D., Vaughan, D.J., 2004. Variations in the compositional, textural and electrical properties of natural pyrite: a review. Int. J. Miner. Process. 74 (1-4), 41–59.

Barker, S.L.L., Hickey, K.A., Cline, J.S., Dipple, G.M., Kilburn, M.R., Vaughan, J.R., Longo, A.A., 2009. Uncloaking invisible gold: use of nanoSIMS to evaluate gold, trace elements, and sulfur isotopes in pyrite from Carlin-type gold deposits. Econ. Geol. 104 (7), 897–904.

Belissont, R., Boiron, M.C., Luais, B., Cathelineau, M., 2014. LA-ICP-MS analyses of minor and trace elements and bulk Ge isotopes in zoned Ge-rich sphalerites from the Noailhac – Saint-Salvy deposit (France): insights into incorporation mechanisms and ore deposition processes. Geochim. Cosmochim. Acta 126, 518–540.

Benedetto, F.D., Bernardini, G.P., Costagliola, P., Plant, D., Vaughan, D.J., 2005. Compositional zoning in sphalerite crystals. Am. Mineral. 90, 1384–1392.

Benning, L.G., Seward, T.M., 1996. Hydrosulphide complexing of Au(I) in hydrothermal solutions from 150–4008°C and 500–1500bar. Geochim. Cosmochim. Acta 60 (11), 1849–1871.

Boucher, S.M., 2011. Ore petrology and alteration of the West Ansil volcanic-hosted Massive sulphide deposit of the Noranda mining camp, Rouyn-Noranda, Quebec: Unpublished M.Sc. thesis, Canada, University of Ottawa, p. 193.

Bowles, J.F.W, Howie, R.A., Vaughan, D.J., and Zussman, J., 2011. Non-silicates: volume 5A. In: Deer, W.A., Howie, R.A., Zussman, J. (Eds.), Rock-Forming Minerals: Geological Society, London, United-kingdom, p. 920.

Brueckner, S.M., Piercey, S.J., Pilote, J.L., Layne, G.D., Sylvester, P.J., 2016. Mineralogy and mineral chemistry of the metamorphosed and precious metal-bearing Ming deposit, Canada. Ore Geol. Rev. 72, 914–939.

Brueckner, S.M., Kline, A.K., Bilenker, L.D., Poole, J., Whitney, M.S., 2021. Mineral chemistry and sulfur isotope geochemistry from tonalite-hosted, gold-bearing quartz veins at hog mountain, southwestern appalachians: implications for gold precipitation mechanism, sulfur source, and genesis. Econ. Geol. 116 (2), 357–388.

Castroviejo, R., Quesada, C., Soler, A., 2011. Post-depositional tectonic modification of VMS deposits in Iberia and its economic significance. Miner. Deposita 46 (5–6), 615–637.

Cheng, X., Yang, F., Zhang, R., Xu, Q., Li, N., 2020. Metallogenesis and fluid evolution of the Huangtupo Cu–Zn deposit, East Tianshan, Xinjiang, NW China: Constraints from ore geology, fluid inclusion geochemistry, H-O–S isotopes, and U–Pb zircon, Re–Os chalcopyrite geochronology. Ore Geol. Rev. 121, 103469.

Cheshire, M.C., Bish, D.L., 2012. Mineralogical and sulphur isotopic evidence for the influence of sulphate-reducing and -disproportionating bacteria on pyrite and marcasite formation in the Georgia kaolins. Clay Miner. 47 (4), 559–572.

Chouinard, A., Paquette, J., Williams-Jones, A.E., 2005. Crystallographic controls on trace-element incorporation in auriferous pyrite from the Pascua epithermal highsulfidation deposit, Chile, Argentina. Canadian Mineral 43 (3), 951–963.

Cook, N.J., Ciobanu, C.L., Pring, A., Skinner, W., Shimizu, M., Danyushevsky, L., Saini-Eidukat, B., Melcher, F., 2009. Trace and minor elements in sphalerite: a LA-ICPMS study. Geochim. Cosmochim. Acta 73 (16), 4761–4791.

de Ronde, C., Humphris, S., Höfig, T., Reyes, A., 2019. Critical role of caldera collapse in the formation of seafloor mineralization: the case of Brothers volcano. Geology 47 (8), 762–766.

Deditius, A.P., Utsunomiya, S., Reich, M., Kesler, S.E., Ewing, R.C., Hough, R., Walshe, J., 2011. Trace metal nanoparticles in pyrite. Ore Geol. Rev. 42 (1), 32–46.

Deditius, A.P., Reich, M., Kesler, S.E., Utsunomiya, S., Chryssoulis, S.L., Walshe, J., Ewing, R.C., 2014. The coupled geochemistry of Au and As in pyrite from hydrothermal ore deposits. Geochim. Cosmochim. Acta 140, 644–670.

Deng, X.H., Wang, J.B., Pirajno, F., Wang, Y.W., Li, Y.C., Li, C., Zhou, L.M., Chen, Y.J., 2016. Re–Os dating of chalcopyrite from selected mineral deposits in the Kalatag district in the Eastern Tianshan Orogen, China. Ore Geol. Rev. 77, 72–81.

Deng, X.-H., Wang, J.-B., Pirajno, F., Mao, Q.-G., Long, L.-L., 2020. A review of Cu-dominant mineral systems in the Kalatag district, East Tianshan, China. Ore Geol. Rev. 117, 103284.

Duuring, P., Hassan, L., Zelic, M., Gessner, K., 2016. Geochemical and spectral footprint of metamorphosed and deformed VMS-style mineralization in the Quinns District, Yilgarn Craton, Western Australia. Econ. Geol. 111 (6), 1411–1438.

Farrand, M., 1970. Framboidal sulphides precipitated synthetically. Miner. Deposita 5, 237–247.

Franklin, J.M., Gibson, H.L., Jonasson, I.R., and Galley, A.G., 2005. Volcanogenic massive sulfide deposits. Economic Geology 100th Anniversary Volume 98, 523–560.

Frenzel, M., Hirsch, T., Gutzmer, J., 2016. Gutzmer, Gallium, germanium, indium, and other trace and minor elements in sphalerite as a function of deposit type-A meta-analysis. Ore Geol. Rev. 76, 52–78.

Fu, J., Hu, Z., Zhang, W., Yang, L., Liu, Y., Li, M., Zong, K., Gao, S., Hu, S., 2016. In situ, sulfur isotopes (δ^{34}S and δ^{33}S) analyses in sulfides and elemental sulfur using high sensitivity cones combined with the addition of nitrogen by Laser Ablation MC-ICP-MS. Anal. Chim. Acta 911, 14–26.

Galley, A.G., Jonasson, I.R., Watkinson, D.H., 2000. Magnetite-rich calc-silicate alteration in relation to synvolcanic intrusion at the Ansil volcanogenic massive sulfide deposit, Rouyn-Noranda, Quebec, Canada. Miner. Deposita 35 (7), 619–637.

Gammons, C.H., Williams-Jones, A., 1995. Hydrothermal geochemistry of electrum; thermodynamic constraints. Econ. Geol. 90, 420–432.

Genna, D., Gaboury, D., 2015. Deciphering the hydrothermal evolution of a VMS system by LA-ICP-MS using trace elements in pyrite: an example from the Bracemac-McLeod Deposits, Abitibi, Canada, and implications for exploration. Econ. Geol. 110 (8), 2087–2108.

Goldfarb, R.J., Taylor, R.D., Collins, G.S., Goryachev, N.A., Orlandini, O.F., 2014. Phanerozoic continental growth and gold metallogeny of Asia. Gondw. Res. 25 (1), 48–102.

Gregory, D.D., Large, R.R., Bath, A.B., Steadman, J.A., Wu, S., Danyushevsky, L., Bull, S. W., Holden, P., Ireland, T.R., 2016. Trace element content of pyrite from the Kapai Slate, St. Ives Gold District, Western Australia. Econ. Geol. 111 (6), 1297–1320.

Gregory, D.D., Cracknell, M.J., Large, R.R., McGoldrick, P., Kuhn, S., Maslennikov, V.V., Baker, M.J., Fox, N., Belousov, I., Figueroa, M.C., Steadman, J.A., Fabris, A.J., Lyons, T.W., 2019. Distinguishing ore deposit type and barren sedimentary pyrite using laser ablation-inductively coupled plasma-mass spectrometry trace element data and statistical analysis of large data sets. Econ. Geol. 114, 771–786.

Gregory, D., Meffre, S., Large, R., 2014. Comparison of metal enrichment in pyrite framboids from a metal-enriched and metal-poor estuary. Am. Mineral. 99 (4), 633–644.

Habicht, K.S., Canfield, D.E., Rethmeier, Jorg, 1998. Sulfur isotope fractionation during bacterial reduction and disproportionation of thiosulfate and sulfite. Geochim. Cosmochim. Acta 62 (15), 2585–2595.

Hannington, M.D., 2014. Volcanogenic massive sulfide deposits. Treatise Geochem. 463–488.

Hannington, M., Harðardóttir, V., Garbe-Schönberg, D., Brown, K.L., 2016. Gold enrichment in active geothermal systems by accumulating colloidal suspensions. Nat. Geosci. 9 (4), 299–302.

Hannington, M.D., Scott, S.D., 1989. Sulfidation equilibria as guides to gold mineralization in volcanogenic massive sulfides: evidence from sulfide mineralogy and the composition of sphalerite. Econ. Geol. 84, 1978–1995.

Huang, J.H., Chen, H.Y., Han, J.S., Deng, X.H., Lu, W.J., Zhu, R.L., 2018. Alteration zonation and short wavelength infrared (SWIR) characteristics of the Honghai VMS Cu-Zn deposit, Eastern Tianshan, NW China. Ore Geol. Rev. 100, 263–279.

Huston, D., Bottrill, R.S., Creelman, R., Zaw, K., Ramsden, T., Rand, S., Gemmell, J.B., Bruce, L., Sie, S.H., Large, R.R., 1992. Geologic and geochemical controls on the mineralogy and grain size of gold-bearing phases, eastern Australian volcanic hosted massive sulfide deposits. Econ. Geol. 87, 542–563.

Huston, D.L., Sie, S.H., Suter, G.F., Cooke, D.R., Both, R.A., 1995. Trace elements in sulfide minerals from eastern Australian volcanic-hosted massive sulfide deposits; part I, Proton microprobe analyses of pyrite, chalcopyrite, and sphalerite, and part II, Selenium levels in pyrite; comparison with delta ^{34}S values. Econ. Geol. 90, 1167–1196.

Hutchison, M.N., Scott, S.D., 1983. Experimental calibration of the sphalerite cosmobarometer. Geochim. Cosmochim. Acta 47 (1), 101–108.

Iizasa, K., Asada, A., Mizuno, K., Katase, F., Lee, S., Kojima, M., Ogawa, N., 2019. Native gold and gold-rich sulfide deposits in a submarine basaltic caldera, Higashi-Aogashima hydrothermal field, Izu-Ogasawara frontal arc, Japan. Mineralium Deposita 54 (1), 117–132.

Janecky, D.R., Shanks, W.C., 1988. Computational modeling of chemical and sulfur isotopic reaction processes in seafloor hydrothermal systems: chimneys, massive sulfides, and subjacent alteration zones. Canadian Mineral 26, 805–825.

Kajiwara, Y., Krouse, H.R., 1971. Sulfur isotope partitioning in metallic sulfide systems. Can. J. Earth Sci. 8 (11), 1397–1408.

Keith, M., Haase, K.M., Schwarz-Schampera, U., Klemd, R., Petersen, S., Bach, W., 2014. Effects of temperature, sulfur, and oxygen fugacity on the composition of sphalerite from submarine hydrothermal vents. Geology 42 (8), 699–702.

Keith, M., Haase, K.M., Klemd, R., Krumm, S., Strauss, H., 2016a. Systematic variations of trace element and sulfur isotope compositions in pyrite with stratigraphic depth in the Skouriotissa volcanic-hosted massive sulfide deposit, Troodos ophiolite, Cyprus. Chem. Geol. 423, 7–18.

Keith, M., Häckel, F., Haase, K.M., Schwarz-Schampera, U., Klemd, R., 2016b. Trace element systematics of pyrite from submarine hydrothermal vents. Ore Geol. Rev. 72, 728–745.

Kerr, D.J., Gibson, H.L., 1993. A comparison of the Horne volcanogenic massive sulfide deposit and intracauldron deposits of the Mine Sequence, Noranda. Quebec. Econ. Geol. 88, 1419–1442.

Kristall, B., Nielsen, D., Hannington, M.D., Kelley, D.S., Delaney, J.R., 2011. Chemical microenvironments within sulfide structures from the Mothra hydrothermal field: evidence from high-resolution zoning of trace elements. Chem. Geol. 290 (1-2), 12–30.

Large, R.R., Danyushevsky, L., Hollit, C., Maslennikov, V., Meffre, S., Gilbert, S., Bull, S., Scott, R., Emsbo, P., Thomas, H., Singh, B., Foster, J., 2009. Gold and trace element zonation in pyrite using a laser imaging technique: implications for the timing of gold in orogenic and Carlin-style sediment-hosted deposits. Econ. Geol. 104 (5), 635–668.

Lee, J.H., Yoo, B.C., Yang, Y.S., Lee, T.H., Seo, J.H., 2019. Sphalerite geochemistry of the Zn-Pb orebodies in the Taebaeksan metallogenic province, Korea. Ore Geol. Rev. 107, 1046–1067.

Li, W., Cook, N.J., Xie, G., Mao, J., Ciobanu, C.L., Fu, B., 2021. Complementary textural, trace element, and isotopic analyses of sulfides constrain ore-forming processes for the slate-hosted Yuhengtang Au Deposit, South China. Econ. Geol. 116 (8), 1825–1848.

Li, X., Zhao, K., Jiang, S., Palmer, M.R., 2019. In-situ U-Pb geochronology and sulfur isotopes constrain the metallogenesis of the giant Neves Corvo deposit, Iberian Pyrite Belt. Ore Geol. Rev. 105, 223–235.

Liu, H., Beaudoin, G., 2021. Dissolution-reprecipitation vs. solid-state diffusion in electrum: examples from metamorphosed Au-bearing, volcanogenic massive sulfide (VMS) deposits. Am. Mineral. 106 (10), 1654–1667.

Liu, Y., Hu, Z., Gao, S., Günther, D., Xu, J., Gao, C., Chen, H., 2008. In situ analysis of major and trace elements of anhydrous minerals by LA-ICP-MS without applying an internal standard. Chem. Geol. 257 (1-2), 34–43.

Longerich, H.P., Jackson, S.E., Gunther, D., 1996. Laser Ablation Inductively Coupled Plasma Mass Spectrometric Transient Signal Data Acquisition and Analyte Concentration Calculation 11(9), 899–904.

Mao, Q.G., Wang, J.B., Xiao, W.J., Fang, T.H., Yu, M.J., Ao, S.J., Zhang, J.E., 2014. Stratigraphic, U-Pb (zircon) and geochemical constraints on magmas, mineralization and geological evolution of the Kalatage district, the central part of Dananhu-Haerlik arc in eastern Tianshan Mountains. Acta Geol. Sin. 88, 885–886.

Mao, Q.G., Wang, J.B., Fang, T.H., Zhu, J.J., Fu, W.W., Yu, M.J., Huang, X.K., 2015. Lead and sulfur isotope studies of sulfides from Honghai VMS-type deposit in Kalatage ore belt of eastern Tianshan Mountains. Mineral Deposits 34 (04), 730–744 in Chinese with English abs.

Mao, Q.G., Wang, J.B., Xiao, W.J., Brian, F., Karel, S., Yu, M.J., Fang, T.H., Li, Y.C., 2018. Mineralization of an intra-oceanic arc in an accretionary orogen: Insights from the Early Silurian Honghai volcanogenic massive Cu-Zn deposit and associated adakites of the Eastern Tianshan (NW China). GSA Bull. 131 (5–6), 803–830.

Marques, A.F.A., Barriga, F., Chavagnac, V., Fouquet, Y., 2006. Mineralogy, geochemistry, and Nd isotope composition of the Rainbow hydrothermal field, Mid-Atlantic Ridge. Mineralium Deposita 41 (1), 52–67.

Martin, A.J., McDonald, I., Jenkin, G.R.T., McFall, K., Boyce, A.J., Jamieson, J.W., MacLeod, C.J., 2021. A missing link between ancient and active mafc-hosted seafoor hydrothermal systems-magmatic volatile infux in the exceptionally preserved Mala VMS deposit, Troodos, Cyprus. Chem. Geol. 567, 120127.

Mathieu, L., 2019. Detecting magmatic-derived fluids using pyrite chemistry: example of the Chibougamau area, Abitibi Subprovince, Québec. Ore Geol. Rev. 114, 103127.

Melekestseva, I.Y., Maslennikov, V.V., Tret'yakov, G.A., Nimis, P., Beltenev, V.E., Rozhdestvenskaya, I.I., Maslennikova, S.P., Belogub, E.V., Danyushevsky, L., Large, R., Yuminov, A.M., Sadykov, S.A., 2017. Gold- and silver-rich massive sulfides from the Semenov-2 Hydrothermal Field, 13°31.13′N, Mid-Atlantic Ridge: a case of magmatic contribution? Econ. Geol. 112 (4), 741–773.

Mercier-Langevin, P., Hannington, M.D., Dubé, B., Bécu, V., 2011. The gold content of volcanogenic massive sulfide deposits. Miner. Deposita 46 (5–6), 509–539.

Mercier-Langevin, P., McNicoll, V., Allen, R.L., Blight, J.H.S., Dubé, B., 2013. The Boliden gold-rich volcanogenic massive sulfide deposit, Skellefte district, Sweden: new U-Pb age constraints and implications at deposit and district scale. Miner. Deposita 48 (4), 485–504.

Pan, Y.S., 2019. The Characteristics of Pyrite of Cu-Zn Deposit and Significance of Mineralization in Huangtupo. Xinjiang University, pp. 1–43 (in Chinese with English abstract).

Pfaff, K., Koenig, A., Wenzel, T., Ridley, I., Hildebrandt, L.H., Leach, D.L., Markl, G., 2011. Trace and minor element variations and sulfur isotopes in crystalline and colloform ZnS. Incorporation mechanisms and implications for their genesis. Chem. Geol. 286, 118–134.

Pirajno, F., Seltmann, R., Yang, Y., 2011. A review of mineral systems and associated tectonic settings of northern Xinjiang, NW China. Geosci. Front. 2 (2), 157–185.

Putnis, A., 2009. Mineral replacement reactions. Rev. Mineral. Geochem 70 (1), 87–124.

Reich, M., Deditius, A., Chryssoulis, S., Li, J.W., Ma, C.Q., Parada, M.A., Barra, F., Mittermayr, F., 2013. Pyrite as a record of hydrothermal fluid evolution in a

porphyry copper system: a SIMS/EMPA trace element study. Geochim. Cosmochim. Acta 104, 42–62.

Román, N., Reich, M., Leisen, M., Morata, D., Barra, F., Deditius, A.P., 2019. Geochemical and micro-textural fingerprints of boiling in pyrite. Geochim. Cosmochim. Acta 246, 60–85.

Sakai, H., Marais, D.J.D., Ueda, A., Moore, J.G., 1984. Concentrations and isotope ratios of carbon, nitrogen, and sulfur in ocean-floor basalts. Geochim. Cosmochim. Acta 48 (12), 2433–2441.

Saravanan, C.S., Hazarika, P., Pal, D., Sen, R., Govindaraj, G., 2020. Pyrite textures and trace element compositions from the granodiorite-hosted gold deposit at Jonnagiri, Eastern Dharwar Craton, India: implications for gold mineralization processes. Econ. Geol. 116 (3), 559–579.

Scott, S.D., Barnes, H.L., 1971. Sphalerite geothermometry and geobarometry. Econ. Geol. 66, 653–669.

Şengör, A.M.C., Natal'in, B.A., Burtman, V.S., 1993. Evolution of the Altaid tectonic collage and Palaeozoic crustal growth in Eurasia. Nature 364, 299–307.

Sharpe, R., Gemmell, J.B., 2002. The Archean Cu-Zn magnetite-rich Gossan Hill volcanic-hosted massive sulfide deposit, Western Australia: genesis of a multistage hydrothermal system. Econ. Geol. 97, 517–539.

Sun, B., Ruan, B., Lv, X., Tuohan, B., Ratchford, M.E., 2020. Geochronology and geochemistry of the igneous rocks and ore-forming age in the Huangtan Au-Cu deposit in the Kalatag district, Eastern Tianshan, NW China: implications for petrogenesis, geodynamic setting, and mineralization. Lithos 368-369, 105594.

Sun, B., Ruan, B., Lv, X., Dai, Z., Mao, C., 2021. Genesis and fluid evolution of the Huangtan Au-Cu deposit in the Kalatag district, Eastern Tianshan, NW China: constraints from geology, geochronology, fluid inclusions, and H-O-S-Pb isotope geochemistry. Ore Geol. Rev. 138, 104408.

Sun, Y., Wang, J.B., Wang, Y.W., Long, L.L., Mao, Q.G., Yu, M.J., 2019. Ages and origins of granitoids from the Kalatag Cu cluster in Eastern Tianshan, NW China: constraints on Ordovician-Devonian arc evolution and porphyry Cu fertility in the Southern Central Asian orogenic belt. Lithos 330–331, 55–73.

Sykora, S., Cooke, D.R., Meffre, S., Stephanov, A.S., Gardner, K., Scott, R., Selley, D., Harris, A.C., 2018. Evolution of pyrite trace element compositions from porphyry-style and epithermal conditions at the lihir gold deposit: implications for ore genesis and mineral processing. Econ. Geol. 113 (1), 193–208.

Williams-Jones, A.E., Bowell, R.J., Migdisov, A.A., 2009. Gold in solution. Elements 5 (5), 281–287.

Wilson, S.A., Ridley, W.I., Koenig, A.E., 2002. Development of sulfide calibration standards for the laser ablation inductively coupled plasma mass spectrometry technique. J. Analyt. Atomic Spectrosc. 17 (4), 406–409.

Wohlgemuth-Ueberwasser, C.C., Viljoen, F., Petersen, S., Vorster, C., 2015. Distribution and solubility limits of trace elements in hydrothermal black smoker sulfides: an in-situ LA-ICP-MS study. Geochim. Cosmochim. Acta 159, 16–41.

Wu, Y.F., Li, J.W., Evans, K., Koenig, A.E., Li, Z.K., O'Brien, H., Lahaye, Y., Rempel, K., Hu, S.Y., Zhang, Z.P., Yu, J.P., 2018. Ore-forming processes of the Daqiao epizonal orogenic gold deposit, West Qinling orogen, China: constraints from textures, trace elements, and sulfur isotopes of pyrite and marcasite, and Raman spectroscopy of carbonaceous material. Econ. Geol. 113 (5), 1093–1132.

XXMCL (Xinjiang Xituo MiningCo. Ltd), 2009. Exploration report of copper and zinc deposit in Huangtupo Mining area, Hami city, Xinjiang. p, 1–115.

Yang, C., Chai, F., Yang, F., Santosh, M., Xu, Q., Wang, W., 2018. Genesis of the Huangtupo Cu–Zn deposit, Eastern Tianshan, NW China: constraints from geology, Rb–Sr and Re–Os geochronology, fluid inclusions, and H-O–S–Pb isotopes. Ore Geol. Rev. 101, 725–739.

Ye, L., Cook, N.J., Ciobanu, C.L., Yuping, L., Qian, Z., Tiegeng, L., Wei, G., Yulong, Y., Danyushevskiy, L., 2011. Trace and minor elements in sphalerite from base metal deposits in South China: a LA-ICPMS study. Ore Geol. Rev. 39 (4), 188–217.

Yu, P.-P., Zheng, Y.i., Wang, C.-M., 2020. Trace elemental and sulfur-lead isotopic variations in metamorphosed volcanogenic massive sulfide (VMS) mineralization systems: an example from the Keketale Pb-Zn(-Ag) deposit, NW China. Ore Geol. Rev. 125, 103685.

Zhang, Y.Y., Sun, M., Yuan, C., Long, X.P., Jiang, Y.D., Li, P.F., Huang, Z.Y., Du, L., 2018. Alternating trench advance and retreat: insights from paleozoic magmatism in the Eastern Tianshan, Central Asian Orogenic Belt. Tectonics 37 (7), 2142–2164.

Zhuang, L., Song, Y., Liu, Y., Fard, M., Hou, Z., 2019. Major and trace elements and sulfur isotopes in two stages of sphalerite from the world-class Angouran Zn–Pb deposit, Iran: implications for mineralization conditions and type. Ore Geol. Rev. 109, 184–200.